The Pennsylvania State University

The Graduate School

Materials Science and Engineering

THE EMERGENT MONOCLINIC PHASE IN $KNbO_3$ DISCOVERED USING OPTICAL SECOND HARMONIC GENERATION

A Thesis in

Materials Science and Engineering

by

Jessica Leung

Submitted in Partial Fulfillment
of the Requirements
for the Degree of

Master of Science

May 2013

The thesis of Jessica Leung was reviewed and approved* by the following:

Venkatraman Gopalan
Professor of Materials Science and Engineering
Thesis Advisor

Susan Trolier-McKinstry
Professor of Ceramic Science and Engineering

Zhiwen Liu
Associate Professor of Electrical Engineering

Joan Redwing
Professor of Materials Science and Engineering
Chair of the Department of Department or Graduate Program

*Signatures are on file in the Graduate School

ABSTRACT

Potassium Niobate ($KNbO_3$) is a ferroelectric material with a perovskite structure that exhibits the same types of phase transitions as $BaTiO_3$. At room temperature, the structure is orthorhombic, with the spontaneous polarization along the $\langle 101 \rangle_{pc}$ direction. Optical Second Harmonic Generation (SHG) microscopy is used to study the domain structures of $KNbO_3$ single crystals at room temperature. In this experiment, a monoclinic phase of $KNbO_3$, which emits a higher SHG signal than that of the orthorhombic phases, was also detected. The monoclinic phase, which results from a small structural distortion of the orthorhombic phase, has enhanced piezoelectric properties that can be useful in the applications of lead-free ferroelectric materials.

In this study, SHG polarimetry was used to study the second harmonic responses of orthorhombic and monoclinic domains in $KNbO_3$, therefore the SHG experiment is described in detail. Through the theoretical modeling of these responses, one can determine the types of domains that were probed. The ratios of the nonlinear optical coefficients were extracted from the theoretical fits for the orthorhombic and monoclinic domains. In addition, the existence of the monoclinic phase was verified with nano-scale scanning X-ray diffraction microscopy, where the relative 2θ center-or-masses of the orthorhombic and monoclinic regions were determined to be ~0.30 and ~0.65 mrad, respectively.

TABLE OF CONTENTS

LIST OF FIGURES

Chapter 1

Chapter 2

Chapter 3

LIST OF TABLES

Chapter 2

Chapter 3

Acknowledgements

I would like to thank Dr. Venkatraman Gopalan for his support and guidance throughout the experimental process. His insight on research has been extremely helpful, and I have learned a lot from his teachings. I am also grateful for the help of Dr. Susan Trolier-McKinstry and Dr. Zhiwen Liu. Even with their busy schedules, they were always readily available to answer my questions.

It has been a pleasure to work with my group members, past and present, at Penn State. Dr. Tom Lummen, Dr. Eftihia Vlahos, Ryan Haislmaier, and Brian VanLeeuwen have been especially helpful in making this thesis possible. I am sincerely appreciative of their generous support.

I would like to thank the Penn State Music community for being so welcoming from the beginning of my time here. I had a fantastic time playing in the musical ensembles; I always looked forward to rehearsals, and I grew as a musician.

I would like to thank my family for their never-ending support and understanding. My parents have always given me the freedom to explore my passions, while my sister is an incredible friend. Finally, I would like to express how lucky I feel to have my friends, near and far, for being great company and for always making the time for me.

Chapter 1 Ferroelectric $KNbO_3$

Potassium Niobate ($KNbO_3$) is a ferroelectric material that exhibits a spontaneous polarization at certain temperature ranges in the absence of an external electric field. It is known for its high piezoelectric response, and has become a material of interest as an environmentally friendly substitute for lead-oxide based ferroelectric applications such as actuators, sensors, and transducers.[1] In addition, recent studies of $BaTiO_3$ (also a ferroelectric material) have shown that at room temperature monoclinic phases have enhanced piezoelectric properties that are highly tunable through varying the temperature, pressure, composition, strain, and fields of the experimental system.[2,3] Since $KNbO_3$ has the same structure as $BaTiO_3$, it is expected to also possess monoclinic phases which have large piezoelectricity. However, one additional advantage of $KNbO_3$ is that it has a higher Curie temperature than $BaTiO_3$, so it could be used for higher temperature applications.[4,5]

1.1 Phase Transitions

$KNbO_3$ has a perovskite structure, where K is a cation with a 1+ charge, Nb is a cation with a 5+ charge, and O is the anion with a 2-. **Figure 1.1** is an ideal structure of $KNbO_3$ in the centrosymmetric cubic phase, where the Nb atom is 6 coordinated to oxygen. In the various phase transitions of a $KNbO_3$, the shift of atoms (primarily in the Nb atom) causes a relative displacement of charges, and as a result, a spontaneous polarization develops.

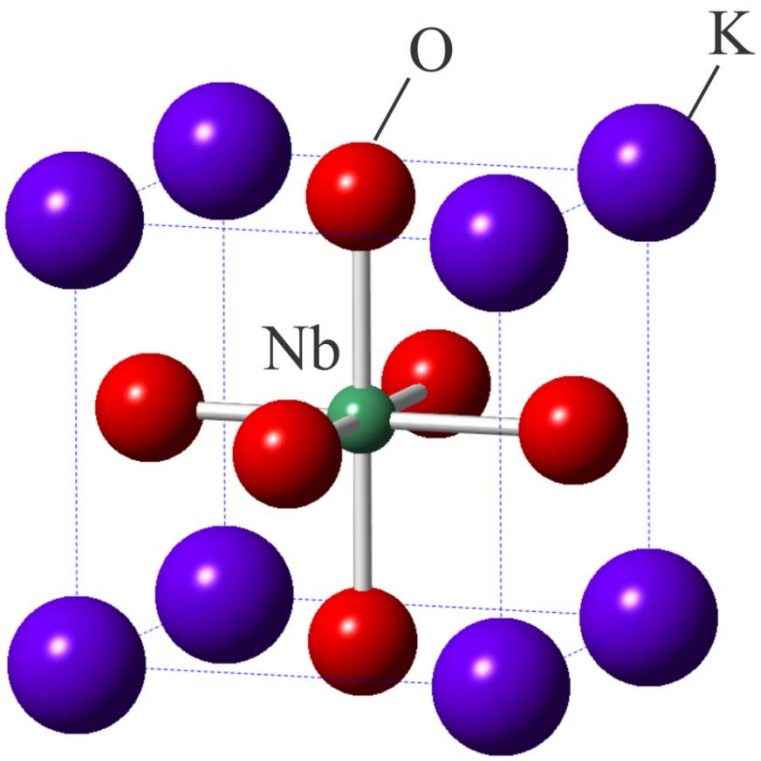

Figure 1.1: The cubic phase of the perovskite, $KNbO_3$, where the unit cell is centered around the Nb atom.

The sequence of the phase transitions in $KNbO_3$ is the same as that of $BaTiO_3$, but the phases transitions occur at different temperatures for each compound. For $KNbO_3$, at temperatures above 435˚ C, the structure is cubic (point group *m*3*m*) and does not exhibit ferroelectric properties (paraelectric). Below 435˚ C, also known as the Curie temperature, the structure is tetragonal (4*mm*) and develops ferroelectric polarization. The structure remains tetragonal between 435 and 225˚ C, but between 225˚C and -10˚C, the material becomes orthorhombic (*mm*2). Finally, below -10˚ C the material becomes rhombohedral (3*m*).[6,7]

The corresponding structural changes due to the phase transitions are illustrated in **Figure 1.2**. The cubic structure is shown in **Figure 1.2 a)**, and the polarization forms in the tetragonal phase (**Figure 1.2 b)**) because there is a displacement of the Nb atom in the

crystal unit cell, therefore the spontaneous polarization (P_S) is along the [001] direction of the cube. In the orthorhombic phase (**Figure 1.2 c)**), the P_S is along the [101] direction of the cube, while the P_S is along the [111] direction of it cubic unit cell in the rhombohedral phase (**Figure 1.2 d)**).[6]

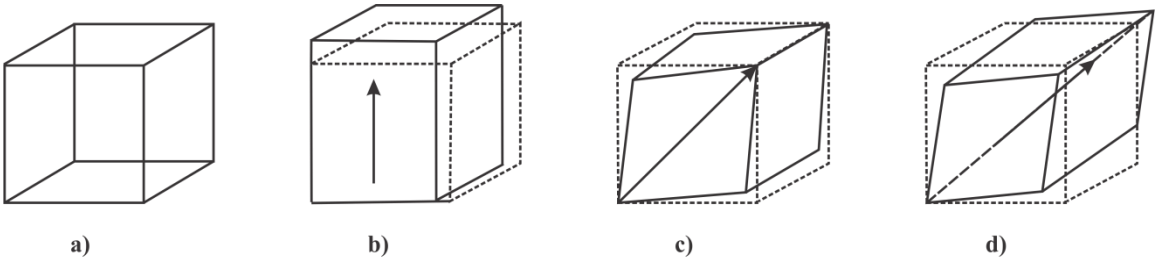

Figure 1.2: The four phases of $KNbO_3$. The a) cubic phase has no spontaneous polarization, and transitions to the b) tetragonal phase with the spontaneous polarization (arrow) along the [001] direction of the cube (dashed lines). The spontaneous polarizations in the c) orthorhombic phase and the d) rhombohedral phase are along the [101] and the [111] directions of the cube.[6]

1.2 Polarization in the Pseudo-Cubic Axes

The $KNbO_3$ sample used in the experiments of this thesis is in the orthorhombic phase. The convention in converting the orthorhombic unit cell into the pseudo-cubic unit cell is that the short axis overlaps with the pseudo-cubic axis of the same direction. The orthorhombic **a**, **b**, and **c** axes can be expressed as [100], [010], and [001], respectively. For convenience and consistency purposes, the *Bmm*2 configuration is adapted to describe the pseudo-cubic conversion of this sample. The **b** axis is parallel to the $[010]_{pc}$ axis, and the **c** axis is chosen along the face diagonal of the $[001]_{pc}$-$[100]_{pc}$ plane in **Figure 1.3**. From here, the polarization direction can be defined in terms of the pseudo-cubic notation.[8]

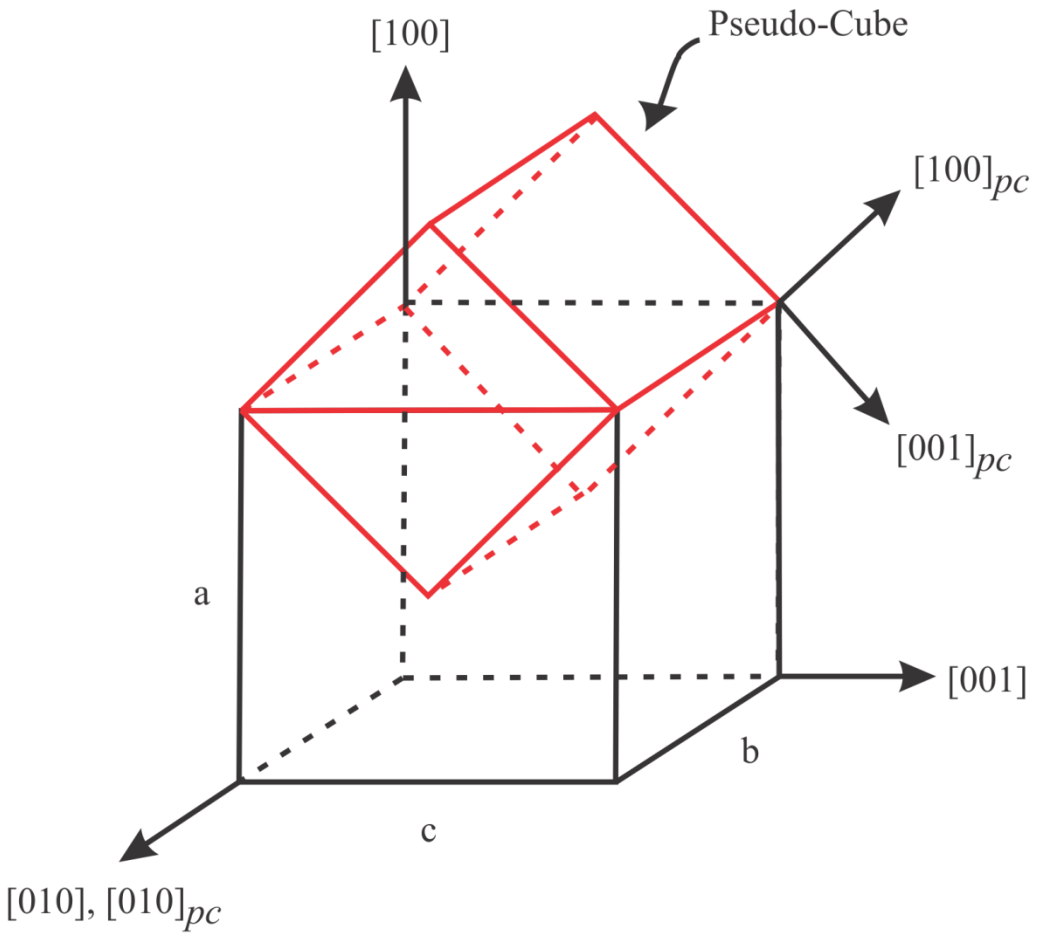

Figure 1.3: This image shows the convention in converting from the orthorhombic unit cell to the pseudo-cubic unit cell for the *Bmm*2 space group. The axes directions with a subscript, *pc*, are the pseudo-cube directions.[8]

As mentioned in Section 1.1, in the orthorhombic phase, the polarization direction can be thought of as along the face diagonals, $<110>_{pc}$, of the pseudo-cube.[6] The sample has many different domains, so the polarization direction changes. Using the orthorhombic notation would be tedious because the coordinate system would change every time a different domain region is probed. Under the pseudo-cubic notation, the polarization direction may change, but it will always be along a set of face diagonal directions.

Since the spontaneous polarization of orthorhombic $KNbO_3$ can lie along the face diagonals of a pseudo-cube, there are twelve possible spontaneous polarization directions. In **Figure 1.4**, the twelve polarization directions are represented by red arrows, and are labeled as **<X,Y,Z>**. The three faces that encompasses the polarizations are the $(100)_{pc}$, $(010)_{pc}$, and the $(001)_{pc}$ faces, indicated in purple, blue, and yellow, respectively. The surface of the sample is along the **X-Y** plane of the laboratory frame, or the $(001)_{pc}$ face. The sample of the surface is equivalent to the (110) face of the orthorhombic unit cell, so the face diagonals of the pseudo-cube is equivalent to the c-axis of the orthorhombic unit cell. Regions of the same type of polarization are defined as domains, and different types of domains are separated by domain walls.

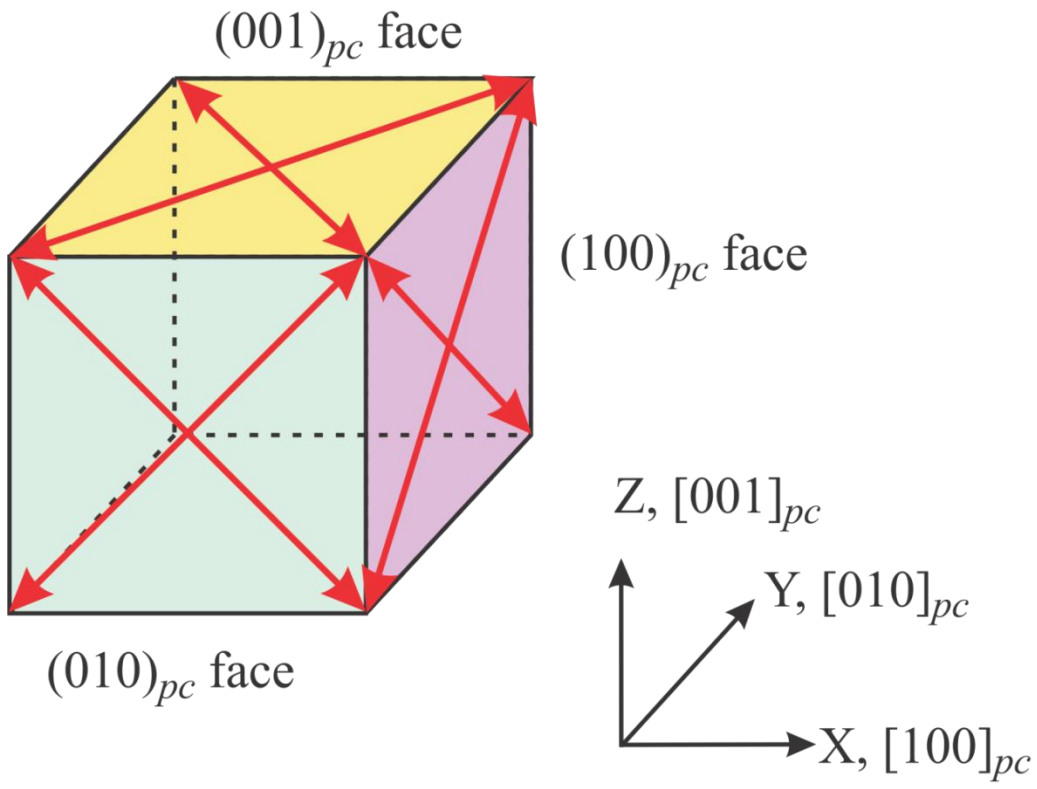

Figure 1.4: The twelve spontaneous polarizations are along the pseudo-cubic faces shown as red arrows in the purple, blue, and yellow and labeled as the $(100)_{pc}$, $(010)_{pc}$, and the $(001)_{pc}$ faces, respectively. The lab axes are the <X,Y,Z> axes. The sample surface is on the X-Y plane, or the $(001)_{pc}$ face.

1.3 Domains and the Allowable Walls

By knowing the various types of polarizations present in an orthorhombic crystal, one can schematically build the allowable domain walls for this phase. In orthorhombic $KNbO_3$, there are four types of domain walls, shown in **Figure 1.5**. The four types of domain walls are the 60˚, 120˚, 180˚, and 90˚ domain walls. The names of the walls indicate the angles between the two polarization directions. In order to have an uncharged wall, which is energetically more favorable than a charged wall, there must be a head-to-tail configuration of the polarization.[6] In this figure, the head is indicated by the arrow, and the tail is the opposite end. The 60° and 120° domain walls are in the $\{110\}_{pc}$ plane, while the 90° and 180° domains walls are in the $\{100\}_{pc}$ plane.[9]

1.4 Second Harmonic Generation

SHG is a type of nonlinear (NL) optical interaction, and is useful in probing a variety of characteristics such as the electronic, vibrational, magnetic, and crystallographic structure of materials.[10] As mentioned previously, ferroelectric materials possess a spontaneous polarization within their crystal structure. As a result of the development of polarization, the inversion symmetry in the cubic form of the perovskite crystal will break and the second harmonic generation signal can be observed. The optical second harmonic generation (SHG) response is sensitive to non-centrosymmetry in materials, making it an ideal technique to probe ferroelectricity in a variety of samples. Therefore, SHG polarimetry can reveal information about local domain structures that

linear optics may not. In this experiment, SHG was used to study the polarization orientation of the ferroelectric material, $KNbO_3$.

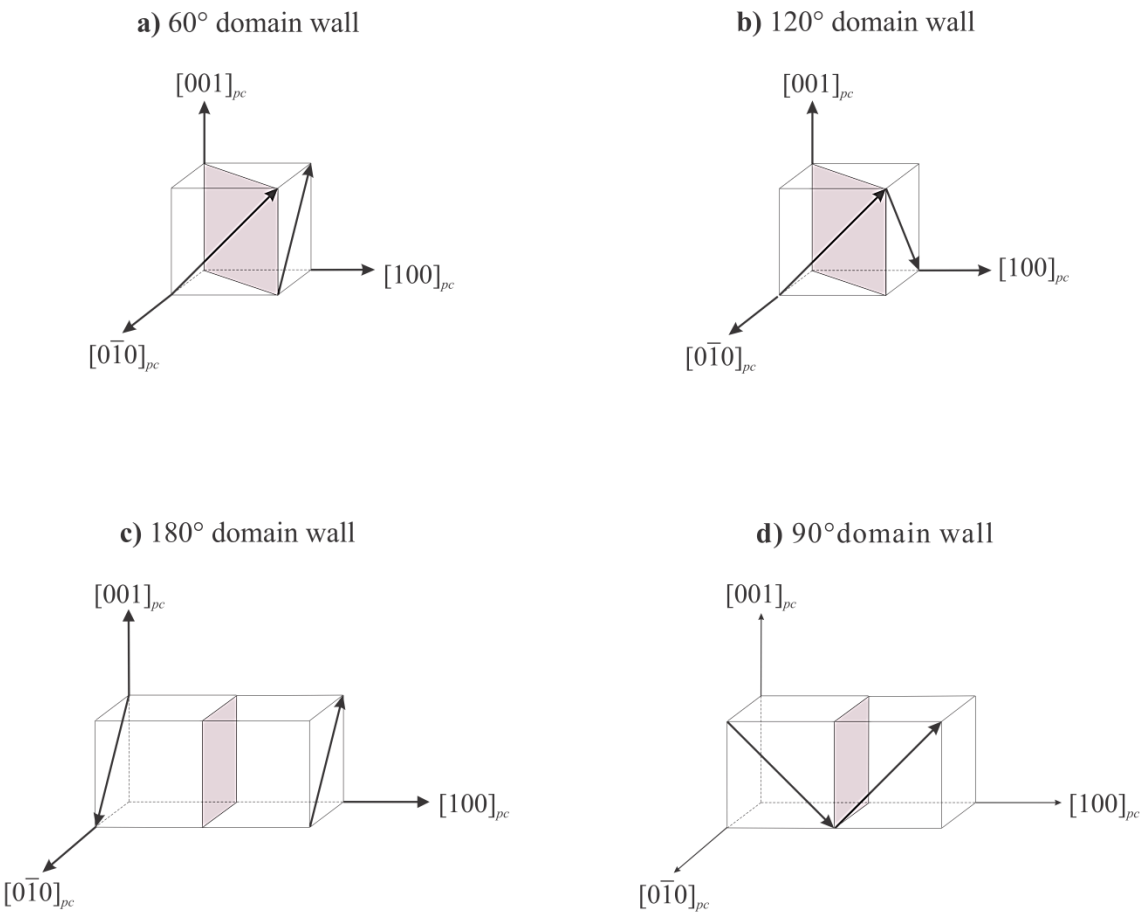

Figure 1.5: The different domain walls (shaded planes) in orthorhombic $KNbO_3$, which includes the a) 60˚ domain, b) 120˚ domain, c) 180˚ domain, and d) 90˚ domain walls. The polarization directions are represented by black arrows. These are just some of the possible configurations of the polarizations in order to generate the walls.[9]

Chapter 2 Sample Preparation

2.1 Sample Orientation

The $KNbO_3$ sample (**Figure 2.1**) was grown and poled by the Oxide Corporation. The only given information of this single crystal was that the crystal axes were along the perpendicular edges of the sample, so the proper space group of this crystal was identified with the help of Laue X-ray diffraction. $KNbO_3$ can be identified as one of three space groups: *Amm*2, *Bmm*2, and *Cm*2*m*, which are different conventions of describing the unit cell. X-ray diffraction was done on each face of the $KNbO_3$ crystal in order to decipher the short axis of the crystal.

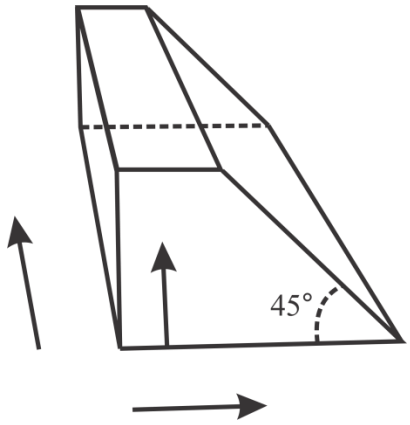

Figure 2.1: The $KNbO_3$ single crystal from the Oxide Corporation. The axes of the crystal are shown with black arrows, but they were unidentified upon reception.

X-ray diffraction normal to the faces of the crystal was used to find its correct space group. The experimental diffraction pattern was compared to the diffraction pattern given by the JPOWD program. By comparing the two patterns the space group should be identified. However, since the room temperature $KNbO_3$ had one significantly short axis of the lattice parameter 3.971 Å, and two longer axes with lattice parameters 5.697 Å and

5.720 Å, it was difficult to differentiate between the two longer axes in a pattern.[11] Therefore we were not able to match the correct space group with the crystal that we received. The beneficial aspect of this X-ray experiment was that the shortest axis was identified, so from that the *Bmm*2 pseudo-cubic naming scheme (Section 1.2) was used.

2.2 Laue X-Ray Diffraction

Laue X-ray diffraction is based on the concept of Bragg's law. When an X-ray beam is incident upon a surface at an angle, only diffraction from certain planes will follow Bragg's law and scatter constructively onto an X-ray detector. Constructively scattering planes are a periodic distance, *d*, apart, while the planes that are not *d* apart will scatter destructively with little to no signal detected.

In the schematic of Bragg's law, shown in **Figure 2.2**, there are incident waves at an angle of incidence, α, from the plane of the sample. Both points *z* and *A* experience the same part of the incoming wave front. Due to geometrical similarities, points *z* and *B* also experience the same part of the incident wave front.[12,13]

According to Bragg's condition, only lattice planes that are a distance, *d*, apart can scatter a constructively interfering wave. Given that distance $\overline{zB}$ is equal to *d*, and that *zAB* is a right triangle, then $\overline{AB}$ is equal to $d\sin\alpha$. Note that points *z* and *C* contain the same part of the wavefront, but the wave traveling to the second plane containing point *B* travels an extra distance of an integral number of waves. The length $\overline{BC}$ is also equal to $\overline{AB}$, so the extra distance traveled by the wave to get to the plane containing

point B is twice the distance $\overline{AB}$, or $2d\sin\alpha$. Finally, due to the constructive interference condition, the extra distance traveled is also equal to $n\lambda$, for the n number of extra waves traveled.

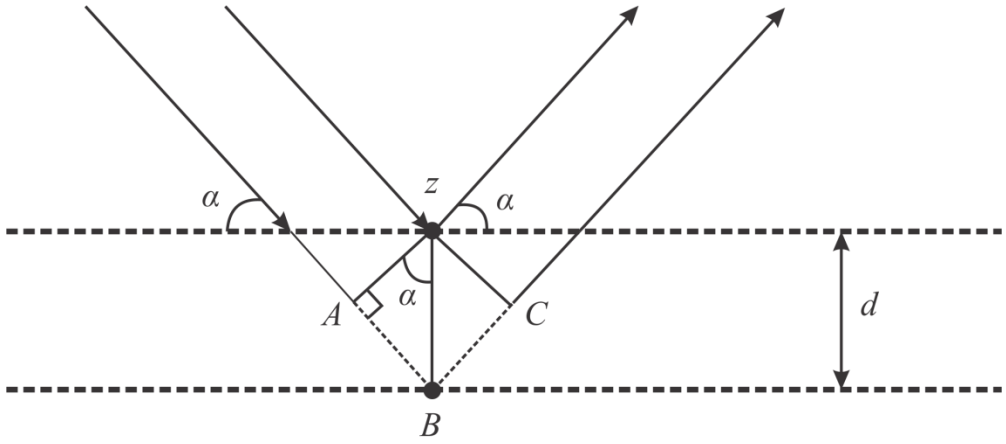

Figure 2.2: A schematic of Bragg diffraction where an X-ray beam is incident upon crystallographic planes (dashed lines) at an angle *α*. The planes are a distance, *d*, apart. The same wavefront exists at points *A*, *B*, *C* and *z*. The diffracted beam also makes an angle *α* from the crystallographic plane. According to Bragg's condition, only certain planes will interfere constructively to form a diffraction pattern.

In order to form a constructively interfering diffraction pattern, the Bragg condition must be fulfilled. This condition is given by,

$$n\lambda = 2d\sin\alpha \tag{1}$$

Note that the corresponding diffraction pattern is unique to the angle of incidence, α, (consequently, the orientation of the sample) and the lattice spacing, d. The symmetry of the diffraction pattern changes depending on the symmetry of the crystallographic plane, therefore it is possible to identify the unknown faces of the sample based on the experimental diffraction pattern. Diffraction patterns also have points of varying intensities. Due to the various wavelengths incident upon a sample, there will be various

planes of different plane distances that reflect back to the detector. In **Figure 2.2**, the distances *AB* and *BC* represent a multiple of the wavelength, λ. This would only happen if the planes containing *z* and *B* were a specific distance, *d*, apart.

In the schematic in **Figure 2.3**, the sample was mounted on a goniometer, which allowed for rotations of the sample. The X-ray was emitted through a hole in the center of the detector screen. For notation purposes, the plane of the sample perpendicular to the X-ray is the **X**-**Y** plane. The Laue equipment is called the Multiwire Back-reflection Laue, manufactured by Multiwire Laboratories, Ltd. It uses a copper source that generates white light radiation. The low power radiation was collimated before approaching the sample. A 30 x 30 cm detector screen, with a hole in the center to emit X-rays, recorded the pattern using the data collection software, NorthStar v6.0.

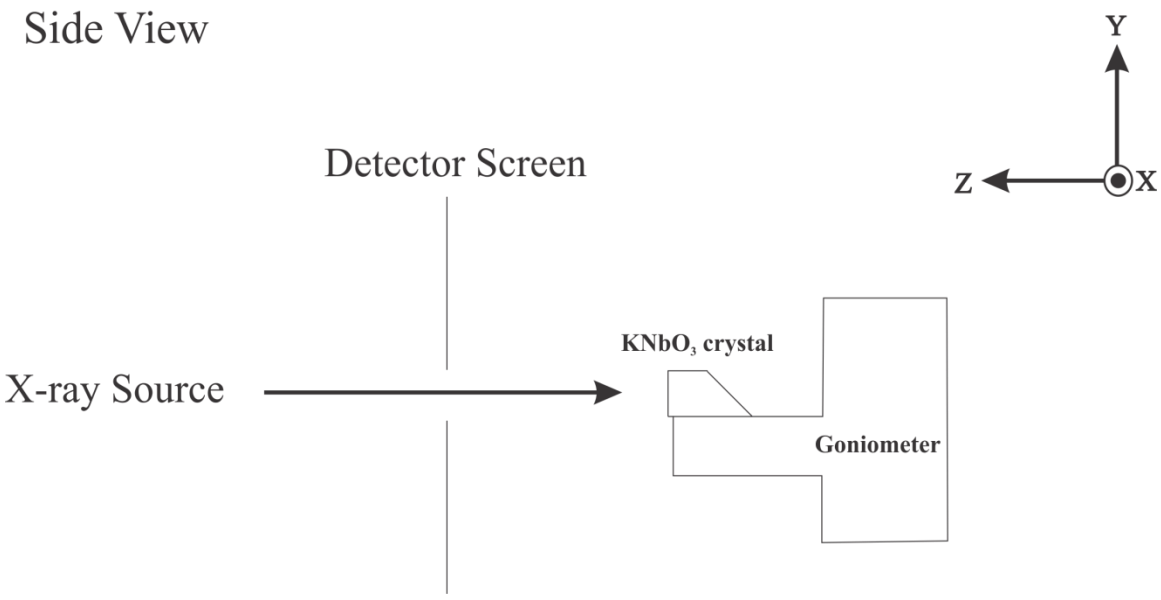

Figure 2.3: The Laue X-ray experimental setup with the $KNbO_3$ crystal glued onto the goniometer. The X-ray that was incident upon the crystal was diffracted off certain crystallographic planes dependent upon Bragg's law. The diffracted pattern was then collected on the detector screen. There is a hole in the center of the screen so that the incident X-ray beam can pass through. The goniometer allowed for the rotation about the X, Y, and Z axes so that the crystal was aligned in order to record a centered diffraction pattern.

2.3 Cutting Samples

The faces of the crystal were labeled A through F. Without slicing the sides of the sample, Laue diffraction would have been difficult to do on face C as labeled in **Figure 2.5**. This was because the face C was 45° from the other faces of the single crystal, causing sample mounting issues. In addition to that, any second harmonic generation (SHG) imaging would have also been difficult due to the need for surface flatness. In order to make this experimental setup more accurate, the crystal faces were sliced off of the bulk crystal.

To ensure that the alignment of each face was correct before cutting, or that the face of the bulk crystal was along a crystallographic plane of the sample, Laue diffraction was done on each face. The crystal was glued (using Crystal Bond) onto a metal rod that inserted into the goniometer. The metal rod was heated to no higher than 225° C (the flow point of Crystal Bond is 125 °F) in order to prevent any phase changes within the crystal. **Figure 2.4 a)** is a schematic of this setup.

The goniometer allowed for rotation along three axes, and once the rotation was done so that the diffraction pattern was centered along the detector. The face was slowly ground down using Grit 320 Si-Carbide paper on a grinding wheel. After this, the face was sliced using the Accutom-2 cutting machine. The cutting speed was set at 0.05 mm/sec. The blade rotation speed was between 200–600 rpm. This process (**Figure 2.4 b**) happened again until all of the faces were aligned and sliced.

Laue X-ray diffraction can be done in reflection or in transmission of the X-ray beam. For the $KNbO_3$ experiments, the back-reflection method was used. The sample

was glued to the edge of the goniometer rod, which allowed for three possible rotations along the **X**, **Y**, and **Z** axes. The **X** and **Y** axes rotations can be noted, while the in-plane rotation along the **Z**-axis cannot be recorded. This would not matter because the in-plane rotation would only rotate the diffraction pattern, but not change the symmetry.

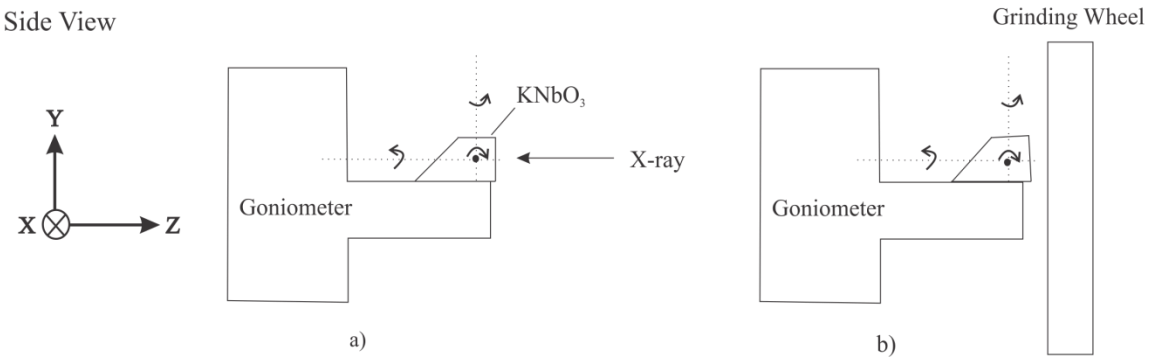

Figure 2.4: a) The crystal on the goniometer with the available rotations shown were about the X,Y, and Z axes in order to align the $KNbO_3$ crystal for a centered diffraction pattern. b) Once the crystal was aligned, the goniometer holding the crystal was pressed against a grinding wheel so that the crystal face was ground down to the crystallographic plane.

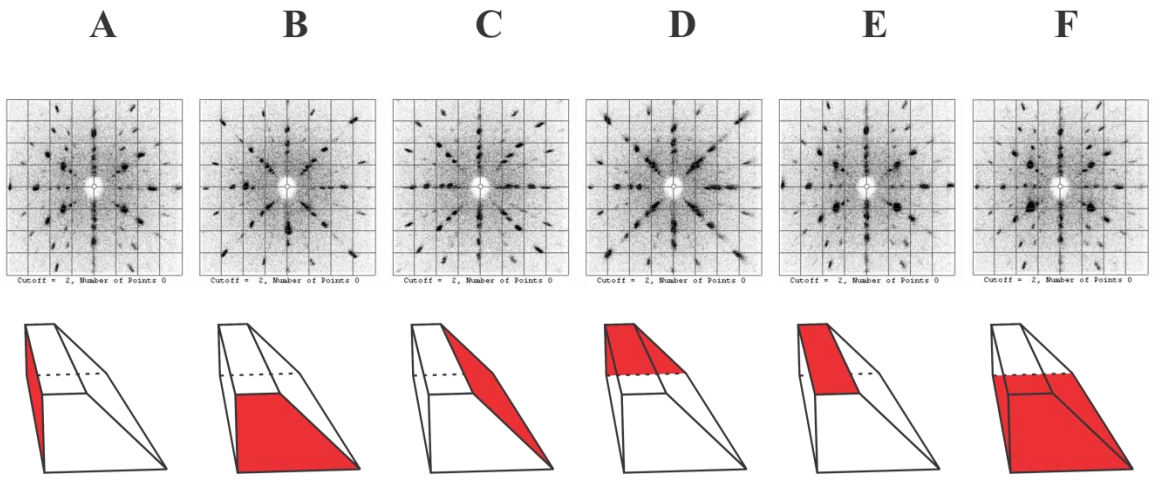

Figure 2.5: The X-ray diffraction patterns of each face of the crystal, labeled A through F and colored in red.

Table 2.1: The parameters of the Laue X-ray Diffraction experiment.

Laue X-Ray Diffraction Parameters	
Collimator Size	1 mm
Source to Sample Distance	121 mm
Collection Time	10 s

2.4 Polishing

After the faces were cut off from the bulk sample, there was one reference side that was initially ground. With the reference side glued to a polishing plate, the non-reference side of the sample was polished to its crystallographic plane. Once this was done, X-ray diffraction was used to check the polished non-reference side of the sample. If the results were acceptable, the reference side was polished next and checked with the X-ray Laue experiment. This process was repeated for each side of the $KNbO_3$ crystal. An in-depth procedure to polishing is as follows.

2.4.1 Mounting a Sample on the Polishing Plate

An aluminum polishing plate (diameter = 10.2 cm) was used to hold the sample and its glass backing. This plate was flattened so that the top and bottom of the plate are parallel to each other. When polishing, the sample was glued using crystal bond onto the center of the plate. The sample was backed up by glass slides so that it created a tiled square as shown in **Figure 2.6**. About six glass squares of ~1.5 cm in length were glued

near the edges of the polishing plate so that the plate was leveled. These squares were distributed evenly around the inner ring of the plate.

Since the $KNbO_3$ samples were about 1.5 mm thick, and the glass slides used for backing were 1 mm thick, two layers of the glass backing were needed. The extra height in glass polished off quickly. It was important to make sure that no air bubbles were trapped beneath the sample or the glass backing because the extra height due to the air bubbles would tilt the polishing. Any glued pieces were pressed down to eliminate air bubbles formed between the glue and the sample/glass, and to make sure that they were flush against the plate.

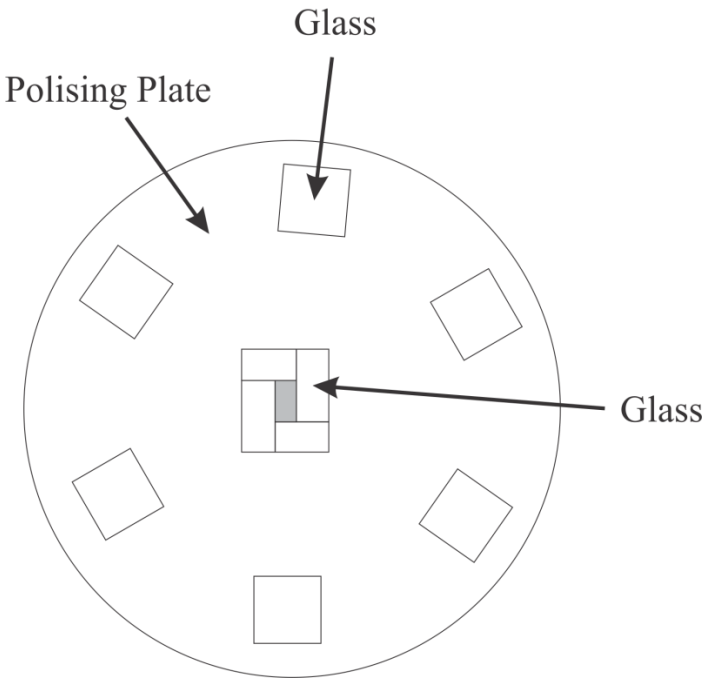

Figure 2.6: The polishing plate with the sample and glass glued onto it. The sample is in the center of the plate, with glass backing around the sample and along the plate edge.

2.4.2 Polishing Technique

SHG measurements were performed in reflection mode, which meant that the sample surface needed to be well polished. The first step in this process was to hand-polish the samples with alumina oxide of different grit sizes. This was done with the polishing plate sample side facing the flat quartz polishing pad.

A small spoonful of 30 μm grit alumina oxide was spread it around the center of the quartz polishing pad. Deionized water was squirted onto the pad so that there was a milky color to the alumina oxide and water slurry. The plate was placed onto the pad (sample facing the mixture) to start the polishing. The polishing motion consisted of pressing the plate firmly onto the pad while making figure eights. The plate was rotated after a few figure eights so that the pressure was distributed evenly throughout the sample. More grit and water were added to the pad when the plate dried.

The polishing was complete when the sample and the glass slides looked uniform in surface roughness under a white light microscope. Before using a lower grit size, the pad and plate were washed off, with soap if necessary, so that the next grit wasn't contaminated. This process was repeated with the 15, 9, and 5 μm grit. After each grit sequence, the surface of the sample would look smoother than the last. When the sequence of grits was completed, the next step was to fine polish the sample using the LOGITECH automatic polisher, model R-2813:1AL52.

On the back of the polishing plate, there was an internal female thread which was used to attach to a plate holder. For the automatic polisher, 0.05 μm colloidal silica (in liquid form) was used. The colloidal silica was poured onto the polishing pad of the

automatic polisher so that the entire surface of the pad was covered. Before setting the plate down onto the pad, the sweeping arm settings were checked. The “Sweeping Arm” option was selected, and the speed was set to 30 rotations per minute. The other speed specifications are listed in **Table 2.2**. The arm should sweep to the edge of the polishing pad. If it did not, then the screw was loosened in order to adjust the polishing arm placement.

After testing the sweeping motion of the polishing arm, the rotation was stopped. The sample was placed facing down onto the pad, while making sure that the plate was snug against the arm. When the arm restarted, the plate moved with the arm during the sweeping motion. At the end of the arm’s sweep, the plate rotated but was still in contact with the arm. Small weights were added to help stabilize the plate when it was rotating. This automatic polishing step continued for about 2-3 hours. After the automatic polishing, the sample looked very smooth under the white light microscope, with no surface roughness visible under reflection. After each side was polished, Laue was used to check if the surface of the sample aligns with the plane of the crystal.

Table 2.2: The settings of the LOGITECH Automatic Polisher.

LOGITECH Polisher Parameters	
Speed	30 RPM
Inner Rotation Speed	26 %
Outer Rotation Speed	100 %
Speed of Pad	80 %

There is an experimental offset from the polishing process that was determined using the Laue X-ray technique. The sample misorientation indicates that the polished face of the crystal is misaligned with the crystallographic plane of the lattice structure.

For the specific piece of crystal used in the SHG experiments, the crystal misorientation was 0.5° in the XY plane, and -0.5° in the YZ plane. The sample misorientation is used in the theoretical modeling of the SHG data.

2.5 Analysis

Figure 2.7 compares the experimental diffraction patterns to the simulated diffraction patterns of the *Bmm*2 space group. When the sample was received, the only information given was that the crystal axes aligned with three of the edges of the sample. The experimental diffraction pattern of side A has a two-fold symmetry, which means that one of the axes is shorter than the other. The shortest axis will have a smaller diffraction plane spacing, *d*, therefore it will have the widest diffraction pattern in reciprocal space.

Table 2.3: The lattice parameters and atom positions used in the JPOWD program to create simulated diffraction patterns

Parameters for the JPOWD Program							
Space Group	a (Å)	b (Å)	c (Å)	Atoms	x	y	z
*Amm*2[14]	3.971	5.694	5.720	K	0	0	0
				Nb	0.500	0	0.510
				O1	0	0	0.490
				O2	0.500	0.253	0.273
*Bmm*2[11]	5.697	3.971	5.720	K	0	0.500	0.517
				Nb	0	0	0
				O1	0	0.500	0.021
				O2	0.254	0	0.285
*Cm*2*m*[15]	5.699	5.720	3.984	K	0	0	0
				Nb	0	0.498	0.500
				O1	0	0.535	0
				O2	0.248	0.280	0.500

The space groups, *Amm*2, *Bmm*2, and *Cm*2*m* contain the short axes with parameters *a*, *b*, and *c*, respectively. The lattice parameters of the different space groups are listed in **Table 2.3**. Each space group is a different description of the same structure, differing only in the labeling system of the lattice parameters. Although we know the shortest axis, it is not possible to identify the intermediate and longest axes through the Laue X-ray diffraction method because the lattice parameters in those directions are too similar to differentiate, therefore the diffraction pattern under the Laue technique looked as if it contained a two-fold symmetry.

In the *Bmm*2 description, face A would be the <100> face. It is not possible to identify this sample of $KNbO_3$ as a particular space group because the simulation patterns are rotated versions of each other. The diffraction pattern will rotate if the plane of the sample is rotated, and since the simulated patterns are along a viewing direction, there is no way of eliminating one space group over the other. However, knowing the shortest axis is enough for the purposes of defining the pseudo-cubic axes used to identify the polarization directions in the phase changes of $KNbO_3$.

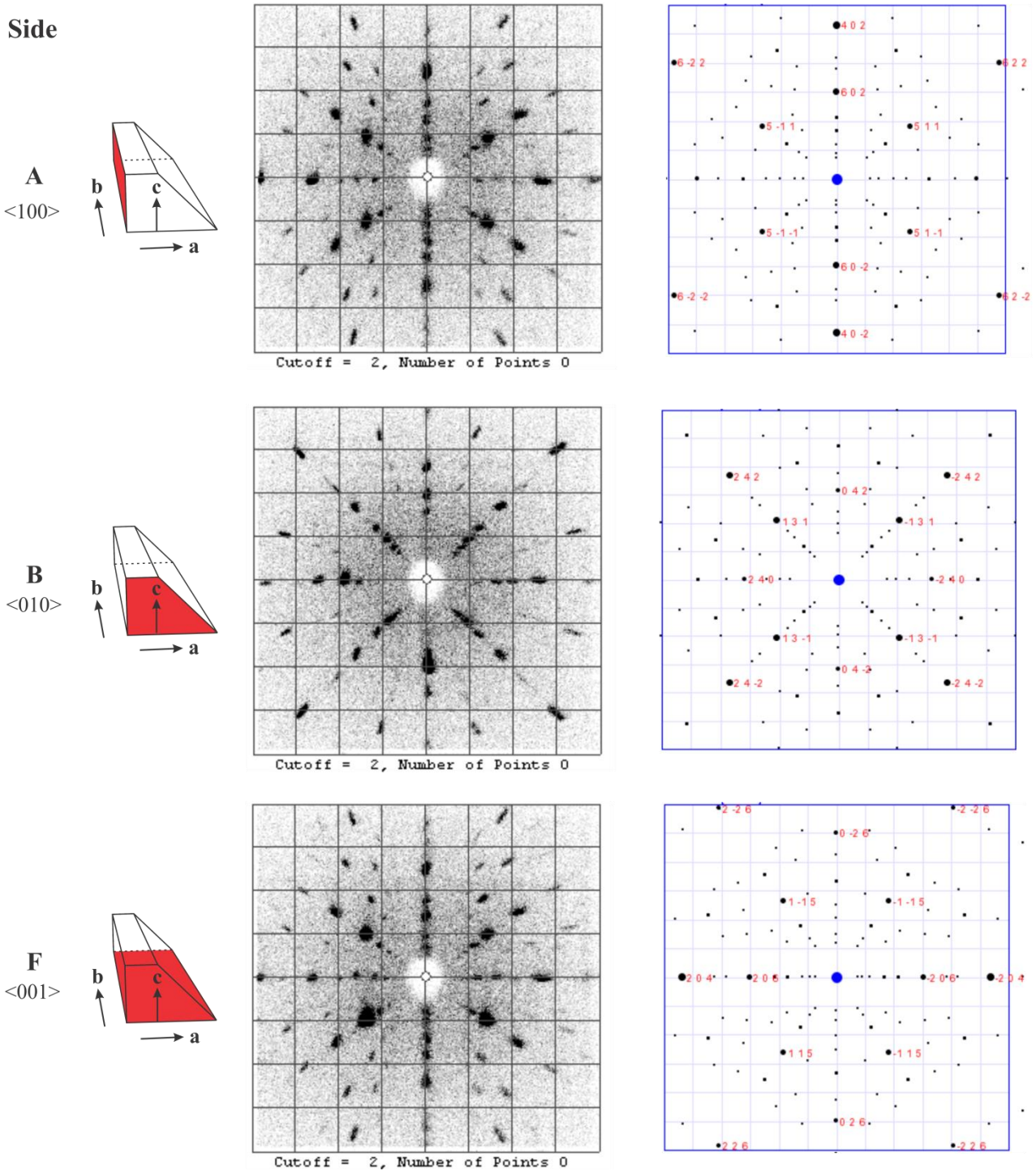

Figure 2.7: The experimental and simulated X-ray diffraction patterns of each face of the $KNbO_3$ crystal.

Chapter 3 Second Harmonic Generation

3.1 Fundamentals

The response of SHG signal can be explained by examining the fundamentals between linear and non-linear (NL) optics. When incoming light is incident upon a material, the electric field component of light interacts with a sample and induces a polarization. In linear optics, the induced polarization is linearly proportional to the electric field. However, in NL optics the polarization also has contributions from higher order terms of the electric field. The linear and higher order contributions to the polarization, P, can be described by,[16]

$$P(t) = P_o + \varepsilon_o \chi_e E(t) + \chi^{(2)} E(t)^2 + \chi^{(3)} E(t)^3 + ..., \quad (2)$$

where P_o is a time independent polarization, ε_o is the permittivity in vacuum, and χ_e is the dielectric susceptibility, which is, $\chi_e = n^2 - 1$, and n is the index of refraction of the material.[17,13] The second order term, $E(t)^2$, corresponds to NL optical processes such as second harmonic generation, sum frequency generation, and difference frequency generation. The $E(t)^3$ term corresponds to third harmonic generation and four-wave mixing.

In optical second harmonic generation, light of a specific fundamental frequency (ω) is incident upon a NL material, and light of a doubled frequency (2ω) is observed using reflection or transmission techniques. In the experiments performed on $KNbO_3$ the measurements were set up in reflection mode, meaning the incident light is at frequency ω, and the reflected frequency is 2ω. A schematic illustrating the incoming and reflected

light in $KNbO_3$ is shown in **Figure 3.1**. In this image, two photons with the frequency ω excite an electron from the ground state to a virtual state. During the de-excitation of the electron, a photon of frequency 2ω is emitted.[16]

3.1.1 Optical Second Harmonic Generation

The NL part of Eq. 2 corresponding to SHG can be rewritten separately as

$$P^{2\omega} = d\left(E^{\omega}\right)^2, \tag{3}$$

where $P^{2\omega}$ is the nonlinear polarization at frequency 2ω induced by the electric field of the fundamental wave, E^{ω}. The term d is the nonlinear coefficient that is conventionally made equal to $\chi^{(2)}$.

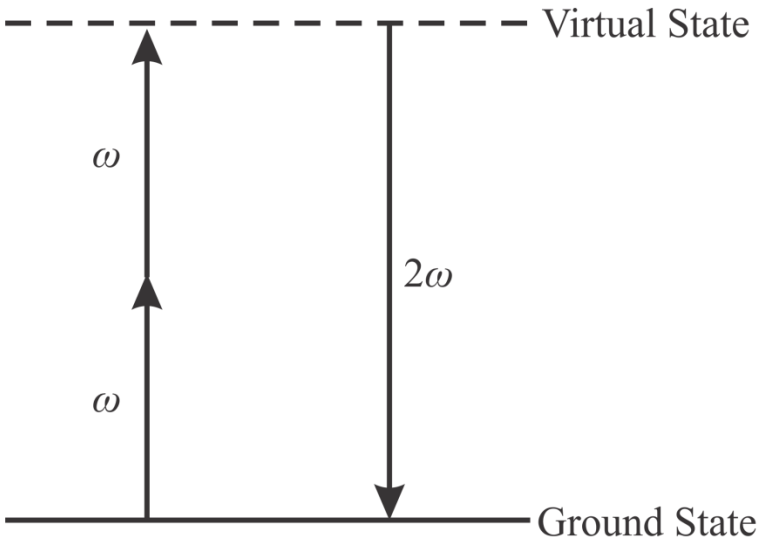

Figure 3.1: A schematic diagram of the optical second harmonic generation process. Two photons of fundamental light of frequency ω excite an electron (up arrows) from the ground state (solid horizontal line) to a virtual (or real) state (dashed horizontal line), which upon de-excitation to the ground state emits a second harmonic photon of frequency 2ω (down arrow).

The tensor form of Eq. 3 is[18]

$$P_i^{2\omega} = \sum_{ijk} d_{ijk} E_j^{\omega} E_k^{\omega} \tag{4}$$

where *i,j,k* represent the directions of polarizations from the electric fields in terms of the crystal physics axes, labeled as *1,2* or *3*. The tensor d_{ijk} is a third rank tensor, but its elements can be truncated using the notation $d_{111} = d_{11}$, $d_{222} = d_{22}$, $d_{333} = d_{33}$, $d_{223} = d_{24}$, $d_{113} = d_{15}$, and $d_{112} = d_{16}$. In addition, by symmetry $E_1E_2 = E_2E_1$, which then indicates that $d_{113} = d_{131}$. The reduced matrix, after applying the above simplifications, can then be written as that shown below. Therefore the matrix form of Eq. 4 is as follows:

$$\begin{pmatrix} P_1 \\ P_2 \\ P_3 \end{pmatrix} = \begin{pmatrix} d_{11} & d_{12} & d_{13} & d_{14} & d_{15} & d_{16} \\ d_{21} & d_{22} & d_{23} & d_{24} & d_{25} & d_{26} \\ d_{31} & d_{32} & d_{33} & d_{34} & d_{35} & d_{36} \end{pmatrix} \begin{pmatrix} E_1^{\,2} \\ E_2^{\,2} \\ E_3^{\,2} \\ 2E_2E_3 \\ 2E_1E_3 \\ 2E_1E_2 \end{pmatrix}. \tag{5}$$

The form of the SHG tensor (or *d*-tensor) is dependent on the point group of the measured material. Some tensor coefficients may not exist due to the symmetries present in its point group. Neumann's Principle can be used to determine which elements exist for a certain point group.[18] The principle states that any macroscopic property tensor of a material must possess *at least* the symmetry of the material's point group.

As was discussed in Chapter 1, $KNbO_3$ at room temperature is orthorhombic and has the point group *mm*2. The two *m*'s in *mm*2 indicate that there are two mirror planes in $KNbO_3$. The first one is called m_1 and refers to a mirror perpendicular to the **1** direction of the crystal physics axes. The second one is called m_2 and refers to a mirror is

perpendicular to the **2** direction of the crystal physics axes. The "2" in *mm*2 indicates that a 2-fold axis exists about the **3** direction in $KNbO_3$. Incidentally, the 2-fold axis is automatically generated from the two mirrors.

One can determine the non-zero coefficient in the *d*-tensor by applying the appropriate transformation matrix to the matrix in question. The following description guides one in the determination of the *d*-matrix for $KNbO_3$ with known point group *mm*2. In considering the first mirror (m_1), the corresponding transformation matrix is[18]

$$a_{m_1} = \begin{pmatrix} -1 & 0 & 0 \\ 0 & 1 & 0 \\ 0 & 0 & 1 \end{pmatrix}. \tag{6}$$

In order to find the SHG tensor, the transformation rule

$$\left(d^{new}\right) = (a)\left(d^{old}\right)\left(a^{transpose}\right) \tag{7}$$

must be applied. Once the first symmetry element (in this case, m_1) is applied, the second mirror (m_2), as well as all other point group symmetry operations must also be applied. By applying Neumann's Principle,

$$\left(d^{new}\right) = \left(d^{old}\right), \tag{8}$$

the final form of the SHG tensor can be determined.

Therefore, for $KNbO_3$ with point group *mm*2, the SHG tensor is[18]

$$d_{mm2} = \begin{pmatrix} 0 & 0 & 0 & 0 & d_{15} & 0 \\ 0 & 0 & 0 & d_{24} & 0 & 0 \\ d_{31} & d_{32} & d_{33} & 0 & 0 & 0 \end{pmatrix}. \tag{9}$$

It is important to note that if a point group contains inversion symmetry, or $\bar{1}$, the SHG tensor will not contain any nonzero elements, hence the material will not generate any SHG signal. This is true for the cubic phase of the perovskite material.

3.2 The SHG Experiment

3.2.1 Experimental Techniques

SHG measurements are generally divided into four different geometries: 1) far-field SHG polarimetry, 2) wide-field SHG interference imaging, 3) near-field SHG microscopy, and 4) scanning SHG microscopy.[10] These four geometries are described below, with an emphasis on 4).

Far-field SHG polarimetry is a table-top experiment that can be performed in either reflection or transmission modes. The fundamental beam is incident upon the sample surface, and the generated second harmonic signal is detected by a photomultiplier tube. Such an experiment is relatively simple to set up, making it a desirable method of measuring SHG. Wide-field SHG interference imaging incorporates the amplitude and phase differences of different domain regions to show contrasts in SHG signal through images. The third technique, near-field SHG microscopy, usually consists of a probe that scans the sample laterally, while collecting scattered light information. This technique gives 10–50 nm resolution, but also gives low signal therefore it is not as widely used.

Scanning SHG, as the name implies, collects a relatively large region of SHG signal by scanning the incoming beam across the sample. The measurements performed on $KNbO_3$ crystals were obtained using scanning SHG microscopy in order to image the ferroelectric domains. In scanning SHG, the fundamental beam is focused onto the sample using a microscope objective, and then the reflected beam is collected by a detector. This method can be used in either transmission or reflection mode. The lateral resolution is 300 –500 nm in the 800–1000 nm wavelength range. An advantage of scanning SHG microscopy is that one can create an image of the domains in an area of the sample with the help of a piezoelectric-stage that scans the sample (see **Figure 3.2**), so that specific domain regions can be probed.

Figure 3.2 depicts a schematic of the SHG setup, which makes up the microscope by Witec, used in this work. The laser of the fundamental beam can have pulse frequencies of a nanoseconds, picoseconds, or femtoseconds. It is important to note that optics with coatings can emit an SHG signal that cannot be differentiated from the SHG signal of the sample. Therefore non-SHG emitting optics must be used throughout the setup in order to make sure that only SHG signal from the sample is being detected.

The polarization of the fundamental beam was determined by a $\lambda/2$ waveplate specific to the fundamental frequency, ω. The $\lambda/2$ waveplate was mounted on a rotation stage, which precisely varied the angle of polarization. Since the fundamental light was prominent even after its reflection off of a second-harmonic generating sample, a variety of filters were used to eliminate the primary beam before it reached the detector. Fluorescence measurements were performed to make sure that the only intensity signal being detected was the SHG signal from the sample.

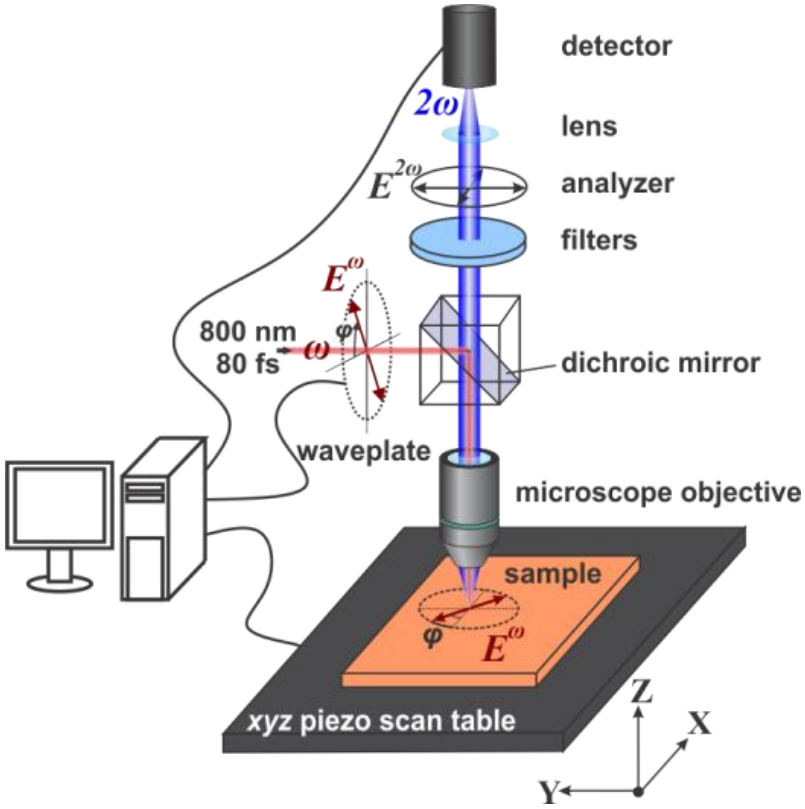

Figure 3.2: The experimental setup of the Witec microscope for optical second harmonic generation experiments.[10] The fundamental electric field was rotated by a $\lambda/2$ plate specific to 800 nm light. The light was reflected downward by a dichroic mirror, and then focused by a microscope objective lens onto the sample. The SHG signal generated by the sample was reflected upward, through the objective lens, and then transmitted through a variety of filters. A polarizer (called the "analyzer") selected the polarization of the SHG signal before the signal reached the detector (a photomultiplier tube). The signal collected by the detector was processed by computer software.

3.2.2 Experimental Setup

The laser setup of the experiment is shown in **Figure 3.3**. The fundamental light was created by a femtosecond pulsed laser called the Tsunami, created by Spectra-Physics.[19] The Tsunami laser was pumped by a diode laser, called the Millennia Xs (Spectra-Physics), which had a power of ~8 W.[20] The Tsunami is a pulsed laser with linear polarization output at a repetition rate of 80 MHz. For experiments, the beam was

externally chopped at ~880 Hz for Lock-in detection. The pulse width was ~80 fs and the average output power was ~1.5 W. The gain medium is Ti: Sapphire, which has a peak intensity emission at around 800 nm, and a tuning range of 690–1080 nm. For this experiment, the laser output was set at 800 nm and the second harmonic signal wavelength was 400 nm.

As mentioned previously, the repetition rate of the beam was modulated through a chopper from 82 MHz to 880 Hz. The beam must be modulated because the available Lock-in amplifier is unable to detect a frequency of 80 MHz. The amplifier can, however, detect the 880 Hz frequency created by superimposing the frequency of the chopper onto the laser beam. The chopper is comprised of a spinning blade that blocks the unwanted pulses and transmits a set number of pulses per second.

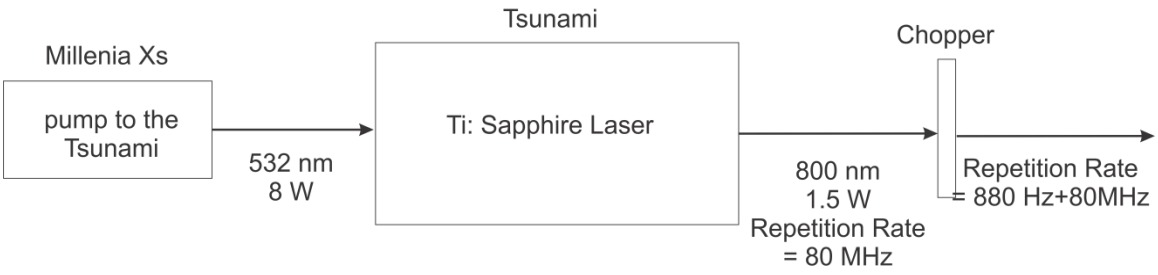

Figure 3.3: The laser layout leading up to the Witec microscope. The Millenia Xs diode laser pumps the femtosecond pulsed Tsunami Ti:Sapphire laser. The output repetition rate was 80 MHz, but a chopper modulated this rate so that the detector can read signal at frequencies of 880 Hz.

The waveplate, as shown in **Figure 3.2**, rotated the electric field of the 800 nm light. After the light leaves the waveplate, the 800 nm wavelength beam reaches a 45° dichroic mirror that reflects the 800 nm light and transmits the second harmonic light. The dichroic mirror is positioned such that the 800 nm light is directed downwards, normal to the sample. The light is focused onto a sample through an objective lens, where 400 nm light is created by the sample and reflected upward while being collimated by the

objective lens. It then approaches the dichroic mirror again, but this time SHG is transmitted, while the residual fundamental light is filtered. The dichroic mirror allows for the 400 nm light to pass through, while filtering some of the residual fundamental light. Additional filters, including a 750 nm shortpass filter, a 400±10 nm bandpass filter, a blue-colored filter, and a neutral density (ND) filter of an optical density (OD) of 2.0, were used. Together, these optics were collectively labeled as "filters" in **Figure 3.2** and are described below.

Filters play an important role in the experimental setup of optics. The 750 nm short-pass filter transmits wavelengths below 750 nm. The 400±10 nm band-pass filter transmits wavelengths in the range of 390 to 410 nm, with a peak transmission of ~31% at 404 nm. The blue filter transmits 400 nm light. Finally, the neutral density (ND) 2.0 filter limits the power density of the fundamental beam so as to not damage the optics, sample, or the measuring electronics. The optical density (OD) number determines the amount of transmission through the filter. For instance, an ND filter with an OD of 2.0 has a fractional transmittance of 10^{-2}, or 10^{-OD}. The optics were chosen after a series of experiments to check the fluorescence of $KNbO_3$, and the process is described in detail in the next section.

A photomultiplier tube (PMT) was required in the SHG experimental setup to amplify and measure the SHG signal. This essential piece is labeled as the "detector" in **Figure 3.2**. When the second harmonic beam reached the PMT, a current signal was created, traveled through a resistor (attached to the Lock-In amplifier), and was measured as a voltage on the Lock-in amplifier. The specific polarization of the induced second harmonic signal, $P^{2\omega}$, was selected by the analyzing polarizer and then detected by the

PMT. The intensity being detected is proportional to the square of $P^{2\omega}$. When the analyzer is set to 0°, only polarizations along the **X** direction are selected. This data is known as I_X. Similarly, the data taken with the analyzer angle at 90° (along the **Y** direction) is called I_Y. From this, one can conclude that the analyzer angle determines the intensity signal detected.

3.3 Eliminating Fluorescence

It is possible for fluorescence to occur within the sample, therefore creating extraneous signal at the PMT that is not due to the second harmonic generation of the crystal. **Figure 3.4 a)** illustrates the absorption and subsequent fluorescence process. In electronic excitation, a photon of energy (E_{photon}), which is wavelength dependent, is absorbed by an electron in the ground state (E_o) and boosts the electron to an excited state (E_1). Most of these excited electrons will relax to an intermediate energy state (E_2). From there, the electrons will either relax further to other intermediate states (such as E_3), or they will emit a photon and return to the ground state. When the electron transitions from E_2 to the ground state (E_o), the process is known as fluorescence. The two sources of signal (SHG and fluorescence) can be differentiated. An example of fluorescence emitted by $CaTiO_3$ is shown in **Figure 3.4 b)**. After shifting the fundamental beam from 800 nm to 825 nm, the peaks seen in the spectra decrease in amplitude; the peaks do not shift in wavelength, therefore fluorescence exists in $CaTiO_3$.

The SHG and fluorescence signals can be distinguished by examining the response of the output wavelength when adjusting the wavelength of the incoming beam.

Second harmonic generation is a fundamental wavelength-dependent technique. By shifting the input wavelength, the signal spectrum also shifts. On the other hand, the fluorescence spectrum increases and decreases in amplitude due to an input wavelength shift. The experiments in this thesis were performed such that the only signal read by the PMT was due to SHG alone. When testing for fluorescence, a spectrometer replaces the photomultiplier tube in the Witec microscope.

The Witec microscope software is known as the "Witec Control." This program can be set up as an oscilloscope for fluorescence measurements, or a scanning control device for SHG measurements. The $KNbO_3$ spectra, was measured to show that fluorescence was eliminated with the use of a 750 nm short-pass filter, a blue-colored filter, and a 400±10 nm band-pass filter.

3.3.1 Fluorescence Experiments Results

Prior to performing any experiments, a background spectrum was obtained. During such a measurement, a spectrum was obtained with the laser turned off in order to measure the background noise in the CCD camera. An example of the background is shown in **Figure 3.5** as the data in black. The spikes in the plots were due to random cosmic rays, so in the figure the signal was around 203 CCD counts. At high wavelengths in the spectrum, a slight increase in CCD counts was observed. The tail is unphysical and is a characteristic of the CCD array. In true SHG, the peak (red curve) shifts by exactly the same amount as the shift in the fundamental wavelength. For the power densities used

in our experiments, the spectrum in **Figure 3.5** shows that $KNbO_3$ crystals did not emit fluorescence.

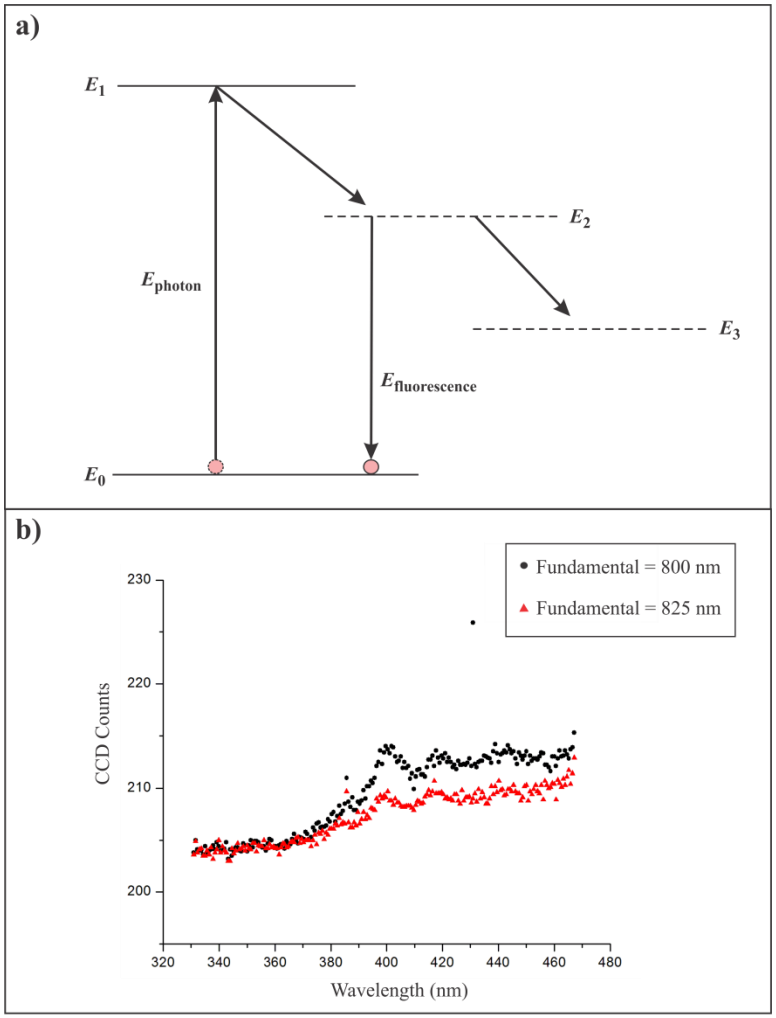

Figure 3.4: a) Fluorescence signal comes from the photon emission between E_2 and E_o, shown as $E_{fluorescence}$. b) An example of fluorescence in $CaTiO_3$. After shifting the fundamental beam from 800 nm to 825 nm, the amplitudes of the peaks decreased, but did not shift, therefore fluorescence was present.

Typically, with SHG measurements, a number of filters are required to ensure the correct wavelength of light is being collected by the CCD camera. More specifically, it is desired to eliminate the fundamental 800 nm beam completely so it does not contribute to the signal at the photomultiplier tube. In this work, SHG experiments were performed using the following optics: a 750 nm short-pass filter, a blue-colored filter, a 400±10 nm band-pass filter, and additional neutral density filters. Collectively, these filters blocked out 800 nm light so that only SHG response was measured by the detector.

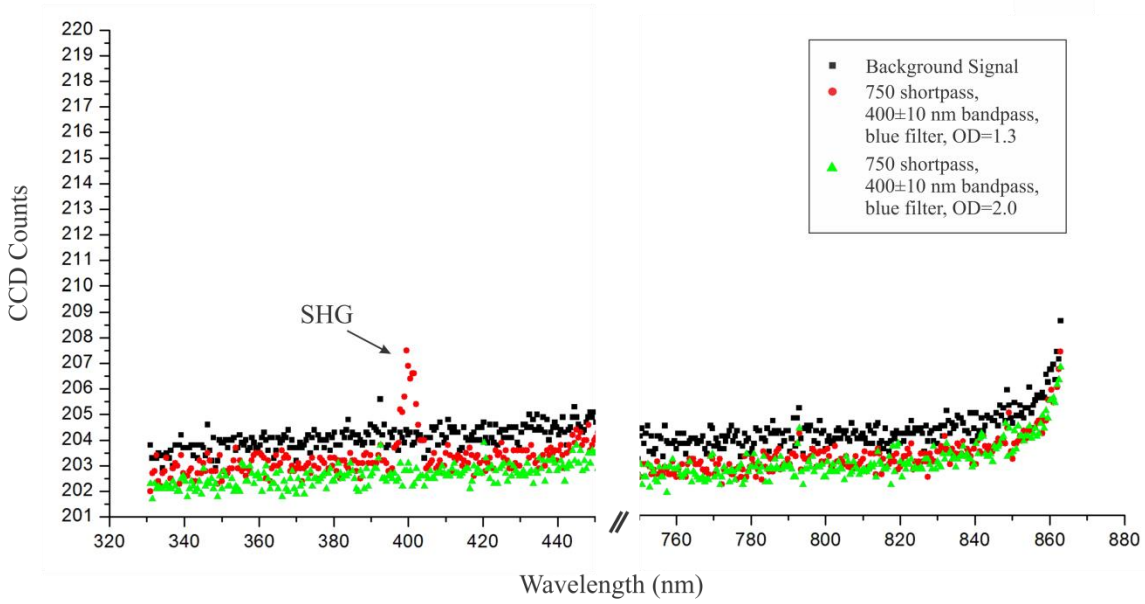

Figure 3.5: The spectra of the background (black), the SHG signal of the $KNbO_3$ crystal with a neutral density (ND), OD=1.3 filter (red), and the SHG signal with an OD=2.0 (green) filter in the setup. In addition to the ND filters, there is also a 750 nm short-pass, a 400±10 nm short-pass, and a blue filter in the optical setup. The peak at 400 nm is the expected SHG signal. When using the listed optics with an OD=2.0 filter, the 800 nm signal was eliminated. Since the PMT is more sensitive than the spectrometer, SHG was detected in the polarimetry experiments. The spectrum data was taken using a spectrometer in place of the PMT in the Witec setup (Figure 3.2).

3.4 Theoretical Model

3.4.1 Reflected SHG

In **Figure 3.6**, consider the fundamental electric field of light, $E_\omega(\phi)$, at frequency ω, at normal incidence to a NL crystal, where ϕ is the in-plane rotation of the fundamental is considered. The reflected SHG intensity, $I^r_{2\omega}$, is detected along either **X**, $[100]_{pc}$, or **Y**, $[010]_{pc}$, as depicted in **Figure 3.6**. An expression for the reflected SHG power, $P^r_{2\omega}$, for a birefringent air/crystal system was derived using the approach given by Herman and Hayden.[21,22] The general form of $P^r_{2\omega}$ at normal incidence becomes,

$$P^r_{2\omega}(\theta = 0^\circ) = \frac{2048\,\pi^3}{c\,A_\omega} P_\omega^{\,2} \frac{{d^r_{eff}}^2}{(1+n_\omega)^2(1+n_{2\omega})^2(n_\omega + n_{2\omega})^2}, \tag{10}$$

where c is the speed of light, A_ω is the area of the fundamental beam spot size, P_ω is the fundamental beam power, d^r_{eff} is the projected SH electric field onto the lab axes, and $n_\omega(n_{2\omega})$ is the refractive index for the fundamental (SH) light.[23,24,25]

By accounting for the for birefringence in the NL crystal, then at any arbitrary angle of ϕ, the index of refraction at any arbitrary angle of ϕ is defined as,[26]

$$n(\phi) = \frac{n_X n_Y}{\sqrt{(n_X \sin\phi)^2 (n_Y \cos\phi)^2}}, \tag{11}$$

where n_X and n_Y are the effective refractive indices along the **X** and **Y** axes, respectively. They are defined with respect to the crystal physics axes $\langle \boldsymbol{a}, \boldsymbol{b}, \boldsymbol{c} \rangle$ for any orientation. For the experiments performed here, the orthorhombic $KNbO_3$ crystal

orientation is defined as ***c*** and ***a*** directions along $\langle 101 \rangle_{pc}$, and ***b*** along $[010]_{pc}$ as shown in **Figure 3.6**.

With this orientation, the effective refractive indices along **X** and **Y** are defined as,

$$n_X = \frac{n_a n_c}{\sqrt{\frac{1}{2}\left(n_a^{\,2} + n_c^{\,2}\right)}} \tag{12}$$

$$n_Y = n_b . \tag{13}$$

The Sellmeier equation used to find the wavelength dependent values of n_a, n_b and n_c can be found in Zysset *et al.* [23]

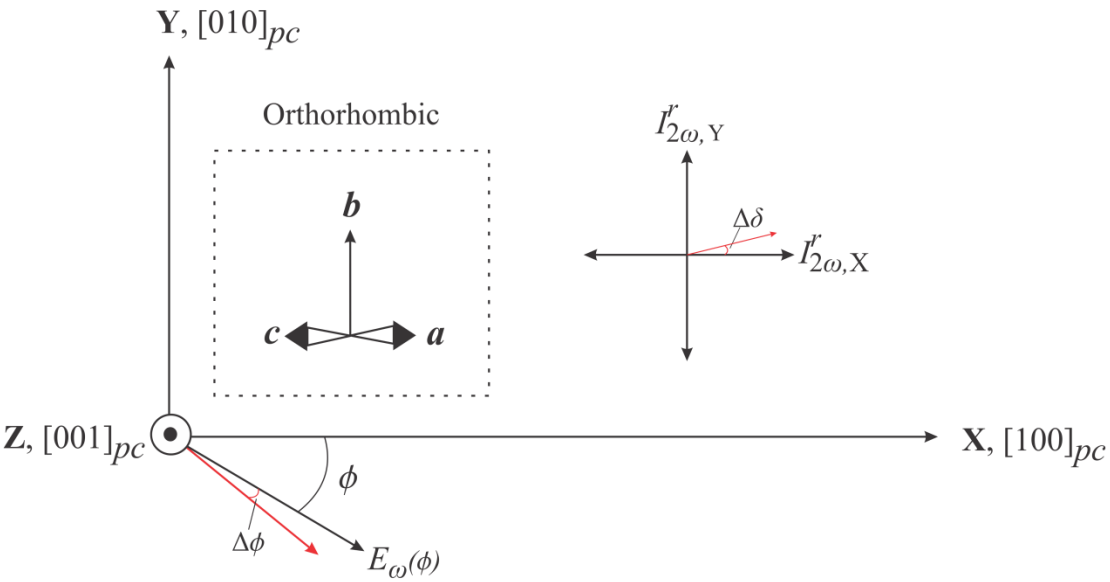

Figure 3.6: The fundamental electric field, E_ω at normal incidence ($\theta = 0^\circ$) creates detected second harmonic intensities, $I^r_{2\omega,X}$ and $I^r_{2\omega,Y}$, along the X and Y lab axes. The orientation of the sample used in the SHG experiment is indicated with the $\langle a, b, c \rangle$ system, while the lab axes are $\langle X, Y, Z \rangle$. The *c*-axis is the polarization direction. The *a* and *c*-axes are oriented at 45° coming out of the X-Y plane as shown by the arrow heads. The angle, ϕ, depicts the rotation of the fundamental electric field from the X-axis. The angles, $\Delta\phi$ and $\Delta\delta$ are the experimental offsets in the waveplate and analalyzer angles, respectively. They are used in the calculations in Section 3.4.2.2.

The d_{eff}^{r} term in Eq. 10 accounts for the NL anisotropy of a material. In general, d_{eff}^{r} is,

$$d_{eff}^{r} = \hat{e}_{2\omega}^{r} \cdot d \otimes \hat{e}_{\omega} \cdot \hat{e}_{\omega}, \tag{14}$$

where, $\hat{e}_{\omega} = \cos\phi\,\hat{\mathrm{X}} - \sin\phi\,\hat{\mathrm{Y}}$ is the vector component of the fundamental electric field in the **X**-**Y** plane as a function of ϕ, $\hat{e}_{X,2\omega}^{r} = \hat{\mathrm{X}}$ ($\hat{e}_{Y,2\omega}^{r} = \hat{\mathrm{Y}}$) is the vector component of the detected SHG intensity along the **X** (**Y**) direction, and d is the transformed d_{ijk} tensor from the orthorhombic (*a*,*b*,*c*) to the lab (X,Y,Z) coordinate system. The function, $\otimes$, is the direct product.

3.4.2 Orthorhombic (*mm*2)

3.4.2.1 Model without experimental offsets

A new *d*-tensor is determined by transforming Eq. 5 using the orientation of the *mm*2 crystal physics axes to the lab axes (X, Y, Z) as shown in **Figure 3.6**. The *d*-tensor becomes

$$d^{mm2} = \frac{1}{2\sqrt{2}} \begin{pmatrix} -(2d_{15} + d_{31} + d_{33}) & -2d_{32} & (2d_{15} - d_{31} - d_{33}) & 0 & (-d_{31} + d_{33}) & 0 \\ 0 & 0 & 0 & 2d_{24} & 0 & -2d_{24} \\ (-2d_{15} + d_{31} + d_{33}) & 2d_{32} & (2d_{15} + d_{31} + d_{33}) & 0 & (d_{31} - d_{33}) & 0 \end{pmatrix}. \tag{15}$$

When considering the three other polarization orientations of the $(010)_{pc}$ face (**Figure 1.4**), it is determined that the *d*-tensors have the same components, but they differ in their signs. Since the SHG intensity expressions are proportional to the polarizations squared,

the intensity expressions for each polarization orientation along this face are degenerate at normal incidence. The four domain orientations are in **Figure 3.7**, where *c* is the polarization direction at 45° above (white arrow with a black arrowhead) or below (black arrow with a white arrowhead) the **X-Y** plane.

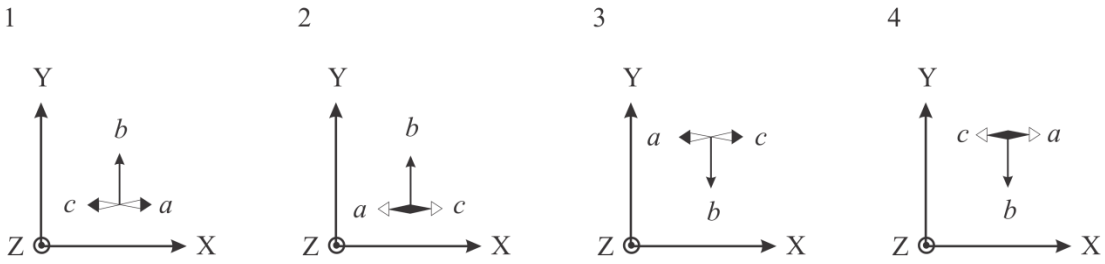

Figure 3.7: The four possible domain configurations of the $(010)_{pc}$ plane, with *c* being the polarization direction. The black arrows with white arrowheads point at 45° into the plane, while the white arrows with black arrowheads point at 45° out of the plane.

By substituting $n(\phi)$ and d back into Eq. 10, the expressions for the SHG intensity along the **X** and **Y** directions are,

$$I_{\mathrm{X},2\omega}^{r,mm2} = \alpha_{\mathrm{X}}\left(\frac{1}{(1+n_{\omega}(\phi))^4(1+n_{2\omega}(\phi))^2(n_{\omega}(\phi)+n_{2\omega}(\phi))^2}\right)\left(\beta(\cos\phi)^2+(\sin\phi)^2\right)^2$$

$$I_{\mathrm{Y},2\omega}^{r,mm2} = \alpha_{\mathrm{Y}}\left(\frac{1}{(1+n_{\omega}(\phi))^4(1+n_{2\omega}(\phi))^2(n_{\omega}(\phi)+n_{2\omega}(\phi))^2}\right)(\sin(2\phi))^2, \quad (16)$$

respectively, where,

$$\alpha_{\mathrm{X}} = \frac{2048\,\pi^3}{c\,A_{\omega}}P_{\omega}^2\left(\frac{d_{32}}{\sqrt{2}}\right)^2,$$

$$\alpha_{\mathrm{Y}} = \frac{2048\,\pi^3}{c\,A_{\omega}}P_{\omega}^2\left(\frac{d_{24}}{\sqrt{2}}\right)^2,$$

$$\beta = \frac{\left(2d_{15} + d_{31} + d_{33}\right)}{2d_{32}} \quad (17)$$

.

The area (A_ω) and power (P_ω) of the fundamental beam are assumed to be constant during all experiments, and therefore are included in the scaling terms, α_{X} and α_{Y}. With these simplifications, there are two scaling parameters, $\alpha_{\mathrm{X}}, \alpha_{\mathrm{Y}}$ and one fitting parameter, β .

3.4.2.2 Model with experimental offsets

The reflected SHG intensity expressions of the orthorhombic phase in Eq. 16 do not include any experimental offsets that exist in both the waveplate and the analyzer (**Figure 3.6**), as compared to the crystal physics axes of the sample. The offset of the waveplate changes the zero setting for the angle of the fundamental electric field with respect to the **X**, $[100]_{pc}$, axis. When there is an analyzer angle offset, additional terms arise in the expressions of the SHG intensity. Due to the offset, the intensity expressions have both the components of $I_{\mathrm{X},2\omega}^{r,mm2}$ and $I_{\mathrm{Y},2\omega}^{r,mm2}$ of Eq. 16. An additional sample misorientation that was found in the Laue experiment should also be included in the model. The intensity offset expression is given by,

$$I_{2\omega}^{r,mm2}(\phi) = \alpha_{\mathrm{X}}\left(\frac{1}{\left(1+n_\omega(\phi)\right)^4\left(1+n_{2\omega}(\phi)\right)^2\left(n_\omega(\phi)+n_{2\omega}(\phi)\right)^2}\right)\mathrm{x}$$

$$\left[\ \left\{\cos^2(\phi+\Delta\phi)\left(-\beta\cos(A1)+\rho\sin(A1)\cos(A2)\right)\right.\right.$$

$$\left.+\sin^2(\phi+\Delta\phi)(\sin(A1)\cos(A2)-\cos(A1))\right.$$

$$+\sin(2(\phi+\Delta\phi))\left(\mu\sin(A1)\sin(A2)\right)\Big\}\cos(\delta+\Delta\delta)$$

$$+\Big\{\cos^2(\phi+\Delta\phi)\left(-\rho\sin(A2)\right)-\sin^2(\phi+\Delta\phi)\sin(A2)$$

$$+\sin(2(\phi+\Delta\phi))\left(\mu\cos(A2)\right)\Big\}\sin(\delta+\Delta\delta)\Big]^2, \tag{18}$$

where,

$$\alpha_{\mathrm{X}}=\frac{2048\,\pi^3}{c\,A_{\omega}}P_{\omega}^2\left(\frac{d_{32}}{\sqrt{2}}\right)^2$$

$$\beta=\frac{\left(2d_{15}+d_{31}+d_{33}\right)}{2d_{32}}$$

$$\rho=\frac{\left(-2d_{15}+d_{31}+d_{33}\right)}{2d_{32}}$$

$$\mu=\frac{d_{24}}{d_{32}}$$

$\Delta\phi$ = waveplate offset angle

δ = analyzer angle

$\Delta\delta$ = analyzer offset angle;

$\delta+\Delta\delta = 0°$ corresponds to $I_{\mathrm{X}}^{r,mm2}$, 90° corresponds to $I_{\mathrm{Y}}^{r,mm2}$

A1 = XZ plane sample misorientation

A2 = YZ plane sample misorientation. (19)

The scaling factor, α_{X}, and the parameter β are the same as those in Eq. 16. The waveplate angle offset, $\Delta\phi$, modifies the incident field angle, ϕ. When the analyzer angle, $\delta = 0^{\circ}$, the existing terms contain $\cos^2(\phi+\Delta\phi)$ and $\sin^2(\phi+\Delta\phi)$, which looks like

$I^{r,mm2}_{X,2\omega}$, and when δ = 90˚, only the $\sin(2(\phi+\Delta\phi))$ term from $I^{r,mm2}_{Y,2\omega}$ exists. When δ is neither 0˚ nor 90˚, there are contributions from both $I^{r,mm2}_{X,2\omega}$ and $I^{r,mm2}_{Y,2\omega}$ as seen in Eq. 18.

3.4.3 Monoclinic (*m*)

As will be shown in the results section of this thesis, the $KNbO_3$ crystals also exhibited an unexpected monoclinic phase. In anticipation of this, a model of a monoclinic system was also derived. The technique to obtain d^r_{eff} for monoclinic symmetry with point group *m*, is the same as the one used for the orthorhombic symmetry described in Section 3.1.1. However, the corresponding *d*-tensor for the monoclinic point group symmetry, *m*, must be used. An example of a monoclinic unit cell with corresponding polarization planes is shown in **Figure 3.7**. The monoclinic symmetry is defined by a single mirror plane containing the polarization, and therefore perpendicular to one of the non-polar crystal physics axes. The monoclinic distortion from the orthorhombic symmetry arises from the destruction of one of the mirror planes in *mm*2, resulting in the loss of the 2-fold symmetry. The remaining mirror plane is either perpendicular to the ***a*** or the ***b*** axis. Therefore, there are two separate possibilities for the monoclinic mirror plane to exist: the $(101)_{pc}$ mirror called m_1, and the $(010)_{pc}$ mirror called m_2, both shown in **Figure 3.8**.

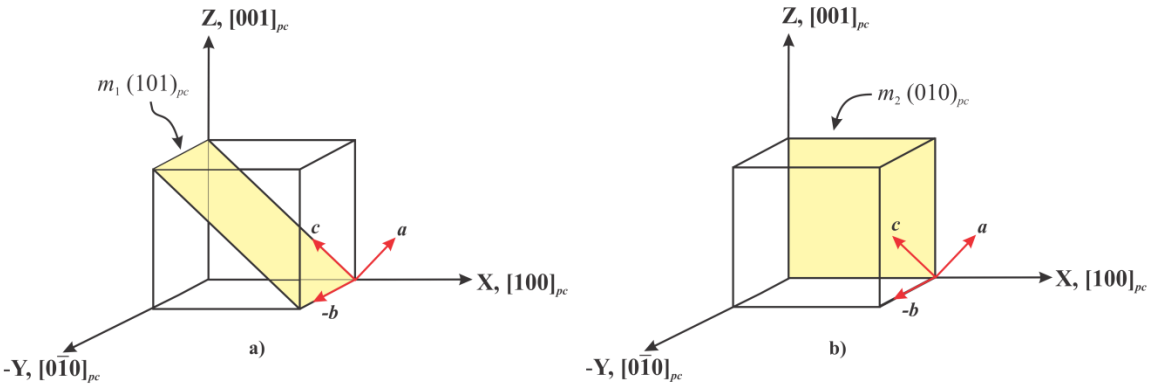

Figure 3.8: The two possible mirror planes that contain the polarization of the monoclinic phase is either in the a) m_1 $(101)_{pc}$ or the b) m_2 $(010)_{pc}$ mirror plane. The polarization can lie anywhere in the mirror planes. The $\langle a, b, c\rangle$ axes are the orthorhombic axes, where *a* and *c* are on the $(010)_{pc}$ face, 45° from the X, $[100]_{pc}$ axis.

For each of the two possible mirror orientations in the monoclinic crystal, the *d*-tensors, d^{m_2} and d^{m_1}, in the crystal physics coordinates (*a*,*b*,*c*) are[18]:

$$d^{m_2} = \begin{pmatrix} d_{11} & d_{12} & d_{13} & 0 & d_{15} & 0 \\ 0 & 0 & 0 & d_{24} & 0 & 2d_{26} \\ d_{31} & d_{32} & d_{33} & 0 & d_{35} & 0 \end{pmatrix} \tag{20}$$

and

$$d^{m_1} = \begin{pmatrix} 0 & 0 & 0 & 0 & d_{15} & d_{16} \\ d_{21} & d_{22} & d_{23} & d_{24} & 0 & 0 \\ d_{31} & d_{32} & d_{33} & d_{34} & 0 & 0 \end{pmatrix}. \tag{21}$$

In addition to the existing *d*-tensor coefficients, there are new coefficients when reducing the symmetry from *mm*2 to *m*. For d^{m_2}, the new coefficients are d_{11}, d_{12}, d_{13}, d_{26}, and d_{35}. The new coefficients that appear in d^{m_1} are d_{16}, d_{21}, d_{22}, d_{23}, d_{24}, and d_{34}. Discussed in the next section, these coefficients show up in the scaling factor expressions as additional terms in the orthorhombic expressions for SHG intensity.

3.4.3.1 The m_2 Mirror

In order to generate the expressions for the reflected SHG intensity for m_2 symmetry, d^{m_2} must be transformed from the orthorhombic axes into the lab axes (X,Y,Z). The transformed tensor is,

$$d^{m_2} = \begin{pmatrix} (d_{11}+d_{13}-2d_{15}-d_{31}-d_{33}+2d_{35}) & 2(d_{12}-d_{32}) & (d_{11}+d_{13}+2d_{15}-d_{31}-d_{33}-2d_{35}) & 0 & (d_{11}-d_{13}-d_{31}+d_{33}) & 0 \\ 0 & 0 & 0 & 2(d_{24}+d_{26}) & 0 & -2(d_{24}-d_{26}) \\ (d_{11}+d_{13}-2d_{15}+d_{31}+d_{33}-2d_{35}) & 2(d_{12}+d_{32}) & (d_{11}+d_{13}+2d_{15}+d_{31}+d_{33}+2d_{35}) & 0 & (d_{11}-d_{13}+d_{31}-d_{33}) & 0 \end{pmatrix} \quad (22)$$

In Section 3.4.2.2, the experimental offsets of the waveplate, analyzer, and sample were incorporated into the orthorhombic model. The same offsets should also be applied to both of the monoclinic models. The m_2 intensity expressions with these offsets are,

$$I_{2\omega}^{r,m_2} = \sigma\left(\frac{1}{\left(1+n_\omega(\phi)\right)^4\left(1+n_{2\omega}(\phi)\right)^2\left(n_\omega(\phi)+n_{2\omega}(\phi)\right)^2}\right)\mathrm{x}$$

$$\begin{aligned}
&\Big[\ \Big\{\cos^2(\phi+\Delta\phi)\big(-D1\cos(A1)-D2\sin(A1)\cos(A2)\big) \\
&+\sin^2(\phi+\Delta\phi)(\cos(A1)+D4\sin(A1)\cos(A2)) \\
&+\sin(2(\phi+\Delta\phi))\big(D3\sin(A1)\sin(A2)\big)\Big\}\cos(\delta+\Delta\delta) \\
&+\Big\{\cos^2(\phi+\Delta\phi)\big(D2\sin(A2)\big)-\sin^2(\phi+\Delta\phi)\big(D4\sin(A2)\big) \\
&+\sin(2(\phi+\Delta\phi))\big(D3\cos(A2)\big)\Big\}\sin(\delta+\Delta\delta)\ \Big]^2,
\end{aligned} \quad (23)$$

where,

$$\sigma = \frac{2048\,\pi^3}{c\,A_\omega}P_\omega^2\left(\frac{d_{12}-d_{32}}{\sqrt{2}}\right)^2$$

$$D1 = \frac{(2d_{15}+d_{31}+d_{33})-(d_{11}+d_{13}+2d_{35})}{2(d_{32}-d_{12})}$$

$$D2 = \frac{(2d_{15} - d_{31} - d_{33}) - (d_{11} + d_{13} - 2d_{35})}{2(d_{32} - d_{12})}$$

$$D3 = \frac{d_{24} - d_{26}}{d_{32} - d_{12}}$$

$$D4 = \frac{d_{12} + d_{32}}{d_{12} - d_{32}}$$

$\Delta\phi$ = waveplate offset angle

δ = analyzer angle

$\Delta\delta$ = analyzer offset angle

$\delta + \Delta\delta$ = 0° corresponds to I_{X}^{r,m_2}, 90° corresponds to I_{Y}^{r,m_2}

A1 = XZ plane sample misorientation

A2 = YZ plane sample misorientation. (24)

The monoclinic SHG intensities in Eq. 23 have identical forms compared to the orthorhombic SHG intensity in Eq. 18. However, the monoclinic parameters of Eq. 24 have the additional *d*-tensor coefficients incorporated into the pre-existing terms from the orthorhombic expressions. The parameter, *D*1, in front of the $\cos^2(\phi + \Delta\phi)$ term, still has the orthorhombic coefficients in the term, $(2d_{15} + d_{31} + d_{33})$, in the numerator, with the monoclinic term, $(d_{11} + d_{13} + 2d_{35})$, subtracted from it. In addition, the parameter *D*3 introduces the new *d*-tensor coefficients, d_{26} and d_{12}. Depending on the relative signs of these additional coefficients, the SHG intensity can increase or decrease, so the general expected shape of the reflection SHG polar plots for the orthorhombic and monoclinic m_2 are qualitatively identical, but the magnitudes are different.

Similar to the orthorhombic model with experimental offset, the m_2 model with offsets have a mixing of pure $I^{r,m_2}_{X,2\omega}$ and $I^{r,m_2}_{Y,2\omega}$. The amount of each component is determined by the analyzer angle, δ. When δ is 0°, only the $I^{r,m_2}_{X,2\omega}$ term contributes to the intensity; when δ is 90°, only the $I^{r,m_2}_{X,2\omega}$ exists. Any other analyzer angle will transmit components of both the intensities.

3.4.3.2 The m_1 Mirror

The reflected SHG intensities for m_1 mirror symmetry are generated in a similar fashion to the expressions of the m_2 mirror symmetry in Section 3.4.3.1. The transformed d^{m_1} tensor from the orthorhombic into the lab axes is,

$$d^{m_2} = \begin{pmatrix} -(2d_{15}+d_{31}+d_{33}) & -2d_{32} & (2d_{15}-d_{31}-d_{33}) & \sqrt{2}(d_{16}-d_{34}) & -(d_{31}-d_{33}) & \sqrt{2}(d_{16}+d_{34}) \\ \sqrt{2}(d_{21}+d_{23}) & \sqrt{2}d_{22} & \sqrt{2}(d_{21}+d_{23}) & 2d_{24} & \sqrt{2}(d_{21}-d_{23}) & -2d_{24} \\ -(2d_{15}-d_{31}-d_{33}) & 2d_{32} & (2d_{15}+d_{31}+d_{33}) & \sqrt{2}(d_{16}+d_{34}) & (d_{31}-d_{33}) & \sqrt{2}(d_{16}-d_{34}) \end{pmatrix}. \quad (25)$$

The m_1 intensity expression with experimental offsets in the waveplate and analyzer is,

$$I^{r,m_1}_{2\omega} = \alpha_X \left(\frac{1}{(1+n_\omega(\phi))^4 (1+n_{2\omega}(\phi))^2 (n_\omega(\phi)+n_{2\omega}(\phi))^2} \right) \times$$

$$\Big[\Big\{ \cos^2(\phi+\Delta\phi)\big(-\beta\cos(A1)+\rho\cos(A2)\sin(A1)+H1\sin(A1)\sin(A2)\big)$$

$$-(2\cos(\phi+\Delta\phi))\big(H3\cos(A1)+H2\cos(A2)\sin(A1)\big)$$

$$+\sin(2(\phi+\Delta\phi))\big(\mu\sin(A1)\sin(A2)\big)$$

$$+\sin^2(\phi+\Delta\phi)\big(-\cos(A1)+\cos(A2)\sin(A1)+H4\sin(A1)\sin(A2)\big)\Big\}\cos(\delta+\Delta\delta)$$

$$+\left\{\cos^2(\phi+\Delta\phi)\left(H1\cos(A2)-\rho\sin(A2)\right)+\sin^2((\phi+\Delta\phi))\left(H4\cos(A2)-\sin(A2)\right)\right.$$

$$\left.+\sin(2(\phi+\Delta\phi))\left(\mu\cos(A2)+H2\sin(A2)\right)\right\}\sin(\delta+\Delta\delta)\Big]^2,$$

(26)

where,

$$\alpha_X=\frac{2048\,\pi^3}{c\,A_\omega}P_\omega^2\left(\frac{d_{32}}{\sqrt{2}}\right)^2$$

$$H1=\frac{\left(d_{21}+d_{23}\right)}{2\sqrt{2}d_{32}}$$

$$\beta=\frac{\left(2d_{15}+d_{31}+d_{33}\right)}{2d_{32}}$$

$$\rho=\frac{\left(-2d_{15}+d_{31}+d_{33}\right)}{2d_{32}}$$

$$\mu=\frac{d_{24}}{d_{32}}$$

$$H2=\frac{\left(d_{16}-d_{34}\right)}{\sqrt{2}d_{32}}$$

$$H3=\frac{\left(d_{16}+d_{34}\right)}{\sqrt{2}d_{32}}$$

$$H4=\left(\frac{d_{22}}{d_{32}}\right)$$

$\Delta\phi$ = waveplate offset angle

δ = analyzer angle

$\Delta\delta$ = analyzer offset angle

(27)

$\delta + \Delta\delta$ = 0° corresponds to I_X^{r,m_1}, 90° corresponds to I_Y^{r,m_1}.

For the m_1 symmetry expressions, the scaling factor, α_X, and the parameter, β, are the same as those of the orthorhombic intensity expression (Eq. 18), but the two types of intensities have different functionalities. Multiplied by the $\cos(\delta + \Delta\delta)$ expression, there is an extra $(2\cos(\phi + \Delta\phi))(H3\cos(A1) + H2\cos(A2)\sin(A1))$ term that was neither present in the orthorhombic nor the m_2 intensity expressions.

As mentioned previously, there are new *d*-tensor coefficients that show up in the d^{m_1} tensor, which were absent in both the d^{mm2} and d^{m_2} tensors. These new coefficients resurface in the parameters, *H*2, *H*3, and *H*4 of Eq. 27. The orthorhombic coefficients of d^{mm2} have been studied, so there are known literature values that can be compared to the ones from the theoretical fits. However, the new coefficients of the monoclinic expressions have not been studied, so the values generated from the following fits cannot be compared to literature.

3.5 Results

3.5.1 Orthorhombic Results

The SHG intensity data taken as a function of the varying input polarization angle, ϕ, as well as the analyzer angle, δ, are known as polar plots. The setup of the Witec microscope allows for the user to select the polar plot locations from an SHG area map shown in **Figure 3.9**. This map is a 79 x 100 μm scan of the SHG intensity of the

$KNbO_3$ $(001)_{pc}$ surface. The scan was collected at 3 data points per 1 μm, with a collection time of 150 ms for each point. A platinum square marker at the top right corner is not SHG active; therefore it shows up as black. The large brown domain regions and the "dagger"-like domains at 45° on the **X**-**Y** plane are orthorhombic domains. The brightest regions with meandering features are the monoclinic domains which we will discuss in Section 3.4.2.

From the region in **Figure 3.9**, polar plots were taken at positions B and C. Shown in the same figure, the polar plots of B and C are similar in that the I_X polar plots are both two-lobed with a slight pinch in the center. The I_Y polar plots of B and C are four-lobed that have finite minima. The theoretical model used to fit this data is in Eq. 16, (without analyzer offsets) which considers the polarization in the $(010)_{pc}$ plane.

The extracted values of the parameter, β, for both B and C can be compared to literature values.[27,24] In literature, β = 1.99 ± 0.25 at 800 nm fundamental light and room temperature, while the average β from the experimental fit is 1.40 ± 7.01 x 10^{-3}. The I_Y polar plots for both positions B and C do not have the four equal lobes as theory would predict. In fact, I_Y has two opposite lobes that are slightly smaller in amplitude compared to the theoretical fit.

The orthorhombic theoretical model fit with offsets in the waveplate, analyzer, and sample misorientation due to the polishing (Eq. 18) is shown in **Figure 3.10**. The sample misorientation discussed in Section 2.4.2 was found using the Laue X-ray diffraction experiment, and was implemented in this fit. The fits of the orthorhombic region also considered polarization in the $(010)_{pc}$ plane since the other planes were

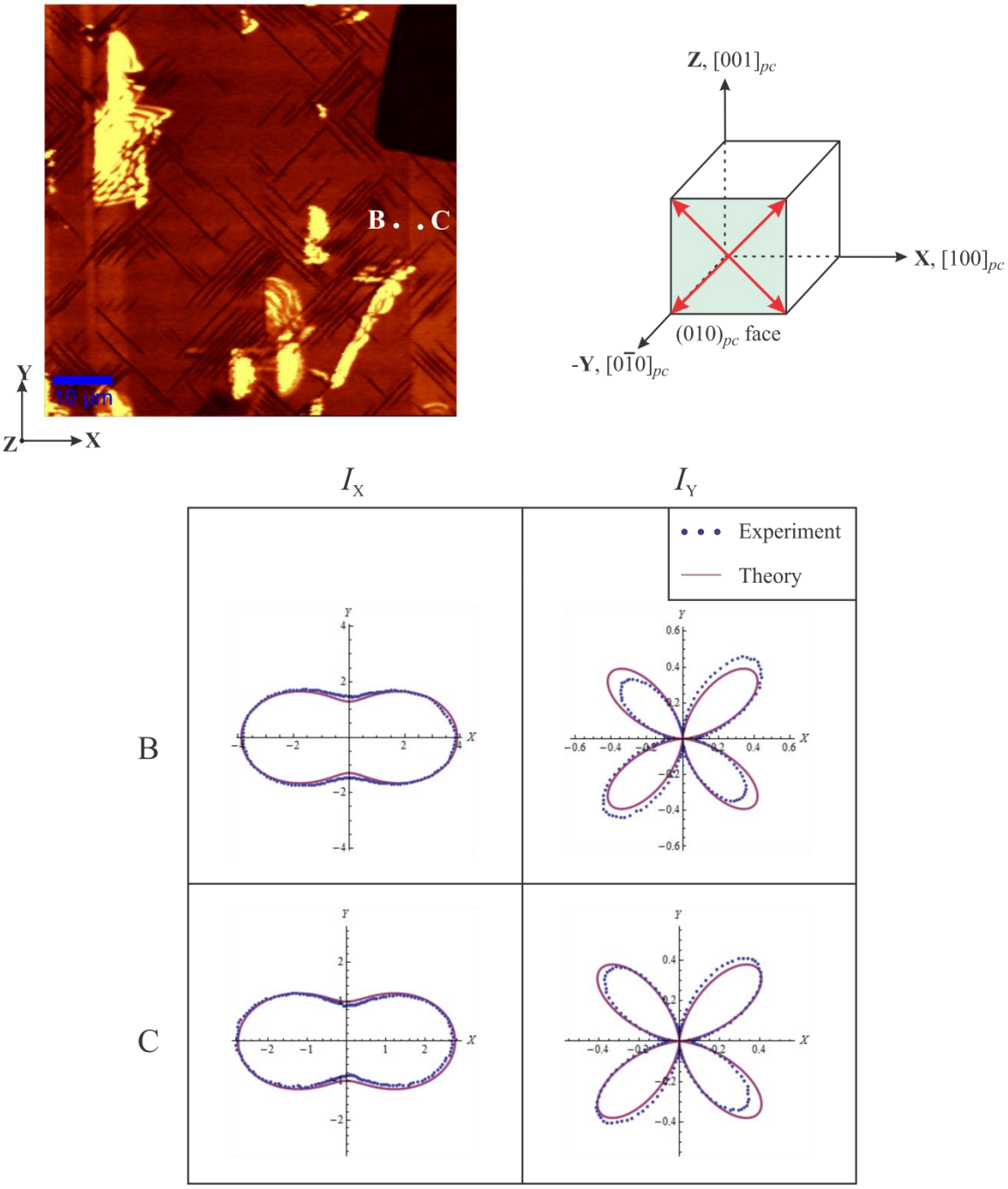

Figure 3.9: The SHG intensity scan of a 79 x 100 µm area on the $(001)_{pc}$ plane. This scan was taken at 3 pts/µm, with a 150 ms/pt. integration time. The orthorhombic regions have features with vertical walls along the $[010]_{pc}$ direction as well as walls at 45° to the $[100]_{pc}$ and $[010]_{pc}$ directions. Bright regions with undefined boundaries are monoclinic regions. Polar plots were taken at positions B and C, which are two different domain regions separated by a domain wall. The fits to the polar plots are from Eq. 16, (without experimental offsets) which considers polarizations in the $(010)_{pc}$ plane. Note that there is a square platinum marker at the top right corner of the scan that is not SHG active.

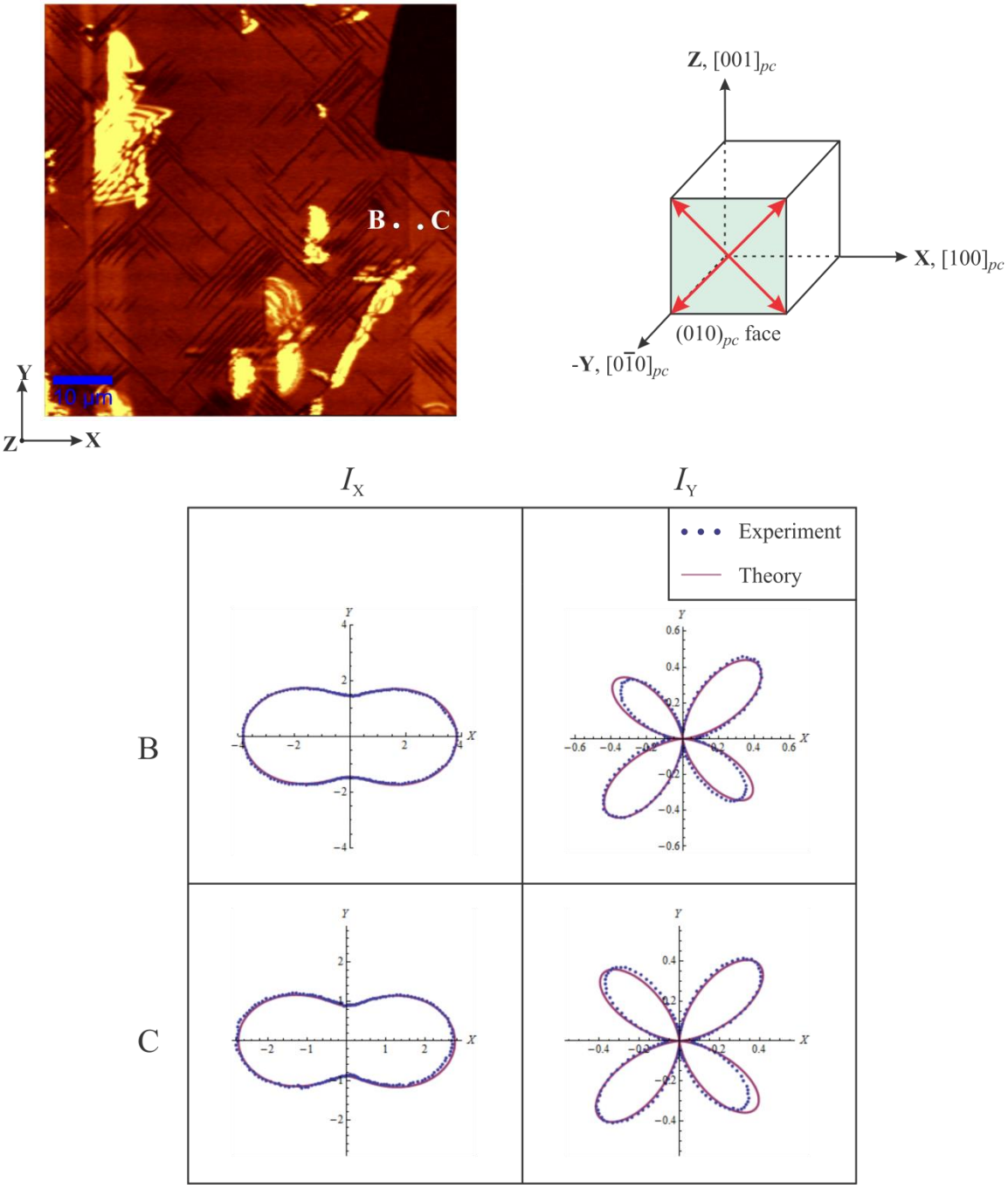

Figure 3.10: The SHG intensity scan of a 79 x 100 µm area on the $(001)_{pc}$ plane. This scan was taken at 3 pts/µm, with a 150 ms/pt integration time. The orthorhombic regions have features with vertical walls along the $[010]_{pc}$ direction as well as walls at 45° to the $[100]_{pc}$ and $[010]_{pc}$ directions. Bright regions with undefined boundaries are monoclinic regions. Polar plots were taken at positions B and C, which are two different domain regions separated by a domain wall. The polar plot of the orthorhombic regions B and C are fitted using the orthorhombic offset model in Eq. 18. Position B and C are from the same SHG intensity map as the one from Figure 3.9. The plane containing the polarization is the $(010)_{pc}$.

eliminated due to poor fits. The unequal lobes can be attributed to the offset that arise in sample offsets. The full list of extracted parameters is shown in **Table 3.1**. The orthorhombic model including offsets fit the unequal lobes of the orthorhombic polar plots. The waveplate offset was $\Delta\phi$ = -1.58 ± 0.048°, and the analyzer offset was $\Delta\delta$ = 0.39 ± 0.073°. These offset values were used to model the monoclinic regions.

Table 3.1: The parameters extracted from the orthorhombic model fit with offsets in the waveplate, analyzer, and sample orientation (Eq. 18). These parameters were generated by implementing the sample offset (due to polishing) angles from the Laue X-ray diffraction experiment.

Parameter	Extracted Parameter	Literature Value
$\beta = \frac{(2d_{15} + d_{31} + d_{33})}{2d_{32}}$	1.39 ± 6.98 x 10^{-3}	1.99 ± 0.25
$\rho = \frac{(-2d_{15} + d_{31} + d_{33})}{2d_{32}}$	2.00 ± 0.670	0.247 ± 9.77 x 10^{-3}
$\mu = \frac{d_{24}}{d_{32}}$	0.628 ± 3.26 x 10^{-3}	0.934 ± 6.65 x 10^{-3}

3.5.2 Monoclinic Results

The monoclinic SHG area map of the monoclinic region is shown in **Figure 3.11**. The dimensions of this scan are 40 x 20 μm at 3 data points per 1 μm, and a 150 ms integration time per point. This monoclinic scan is different from the one orthorhombic scan in **Figure 3.9**, but there are similar features such as the bright intensity and the

meandering domain walls. The monoclinic polar plots were taken at positions F and G of this scan, where F is in a dark band and G is in a bright band in this monoclinic region.

The polar plots of the monoclinic regions, F and G are shown in **Figure 3.11**. The I_X polar plots for F and G are two-lobed with an even more pinched in center that those of the orthorhombic I_X polar plots. Both of the I_Y polar plots are four-lobed and have nonzero minima. The fits of the polar plots using the m_2 (Eq. 23) theoretical models are also in the same figure. Due to the m_1 model having more parameters than the m_2 model, the m_1 model will most certainly fit the polar plot data. However, the two intensity expressions have the same form, therefore only the m_2 mirror is considered in the theoretical fits of the data.

The waveplate offset, $\Delta\phi$ = 1.30 ± 0.060°, and the analyzer offset, $\Delta\delta$ = -0.13 ± 0.030°, were determined earlier from the orthorhombic fits. These values were implemented in the monoclinic fits with the m_2 model. From the m_2 model fit, the extracted parameters are shown in **Table 3.2**. None of the parameters can be compared to literature because they contain new *d*-tensor coefficients that have not been previously studied.

Besides the polar plots taken from positions F and G, polar plots from other positions were also taken. In **Figure 3.12**, the I_X of the orthorhombic region (position A) is plotted with the monoclinic bright (positions G and I) and monoclinic dark bands (positions F and L). The red plot is from the orthorhombic region, containing the least intensity. The medium intensity plots, in brown, are from the dark bands, while the largest intensity plots, in blue, are from the bright bands of the monoclinic region.

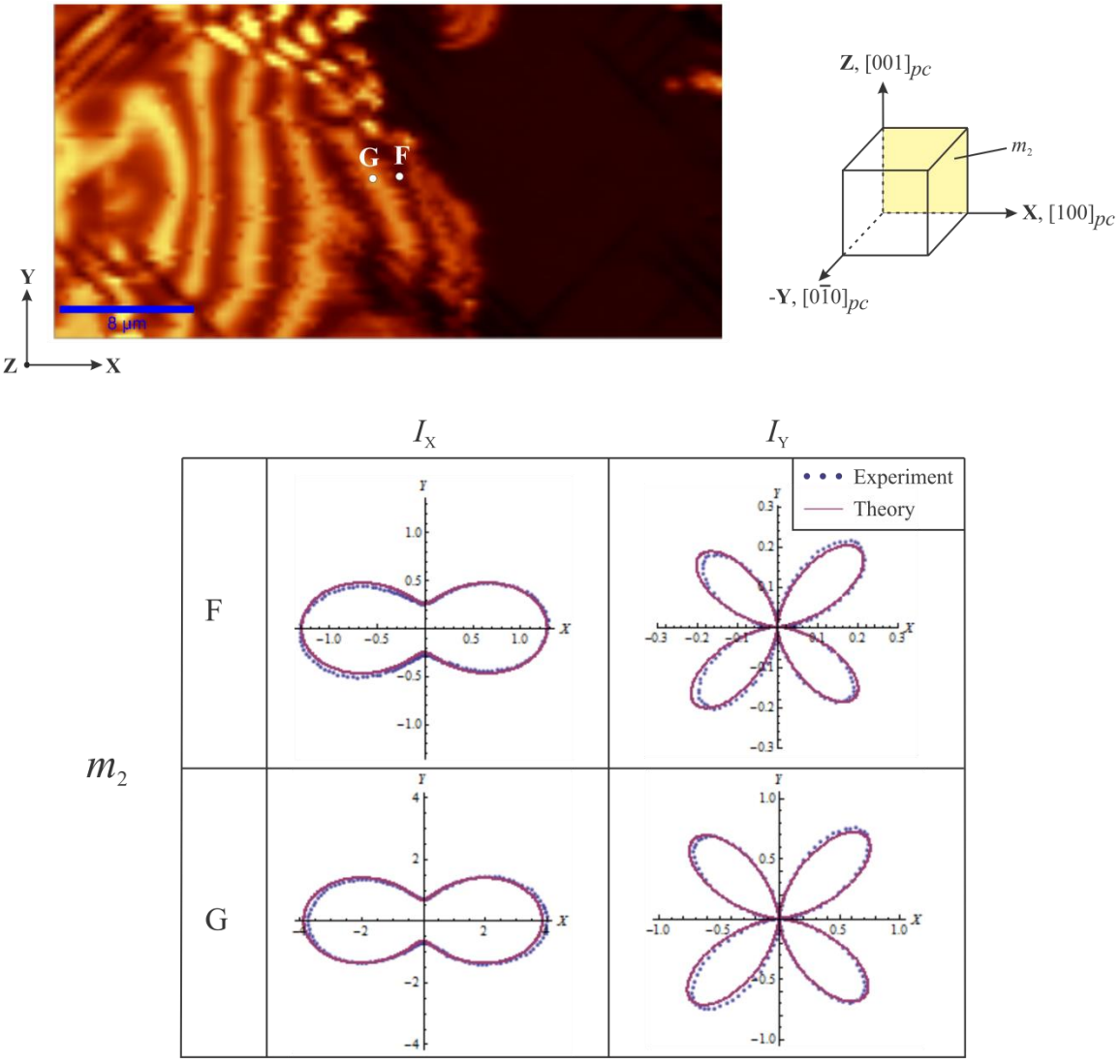

Figure 3.11: A 40 x 20 µm SHG intensity map of a monoclinic region consisting of dark and bright bands. This was taken at 3 pts/µm, with a 150 ms/pt integration time. The scan area is in the $(001)_{pc}$ plane. The dark region is F and the bright region is G. The fits of the monoclinic data consider both the m_2 theoretical model with experimental offsets in the waveplate, analyzer, and the sample polishing.

Table 3.2: The parameters extracted from the m_2 model (Eq. 23) fit with experimental offsets in the waveplate, analyzer, and sample. These parameters were generated by implementing the offset angles found from the orthorhombic model (Eq. 18) fit.

Parameter	Extracted Parameter from m_2 fit
$D1 = \frac{(2d_{15} + d_{31} + d_{33}) - (d_{11} + d_{13} + 2d_{35})}{2(d_{32} - d_{12})}$	1.99 ± 0.034
$D2 = \frac{(2d_{15} - d_{31} - d_{33}) - (d_{11} + d_{13} - 2d_{35})}{2(d_{32} - d_{12})}$	5.31 ± 1.17
$D3 = \frac{d_{24} - d_{26}}{d_{32} - d_{12}}$	1.00 ± 0.015
$D4 = \frac{d_{12} + d_{32}}{d_{12} - d_{32}}$	-5.41 ± 1.31

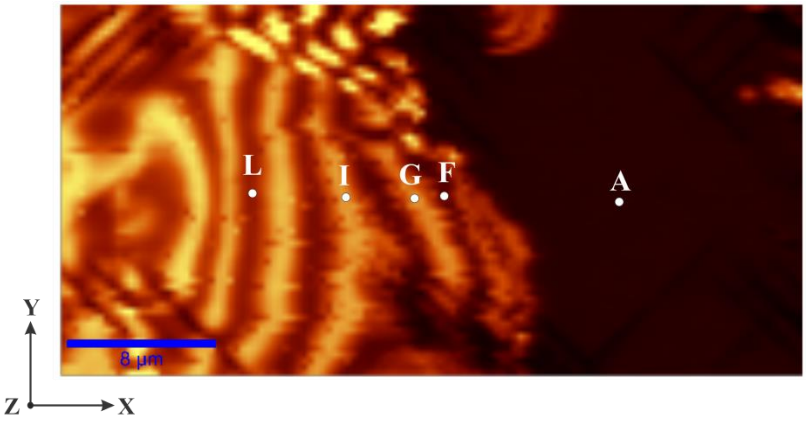

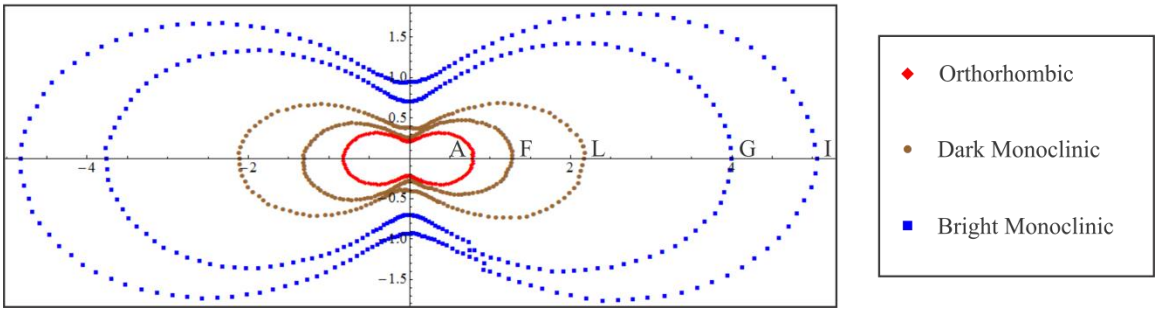

Figure 3.12: An intensity comparison of the I_x polar plots from the orthorhombic (A), dark monoclinic (F and L), and the bright monoclinic (G and I) regions. The lowest intensity comes from the orthorhombic region, the medium intensity from the dark monoclinic regions, and the highest intensity is from the bright monoclinic regions.

3.6 Discussion

3.6.1 Orthorhombic Discussion

Since regions B and C have similarly shaped polar plots, one may suspect that they have similar domains, but B and C are actually from two different domain regions. Upon closer examination, one can see that a domain wall exists between the two regions. A zoomed-in image of regions B, C, and the wall between the two, is shown in **Figure 3.13**. The exaggerated intensity contrast of the zoomed-in region is due to the rescaling of the SHG scan. As discussed in Section 3.4.2.1, the $(010)_{pc}$ in **Figure 3.7** has four polarization directions that give degenerate polar plots, therefore it is possible to have different domain regions that have similar polar plots.

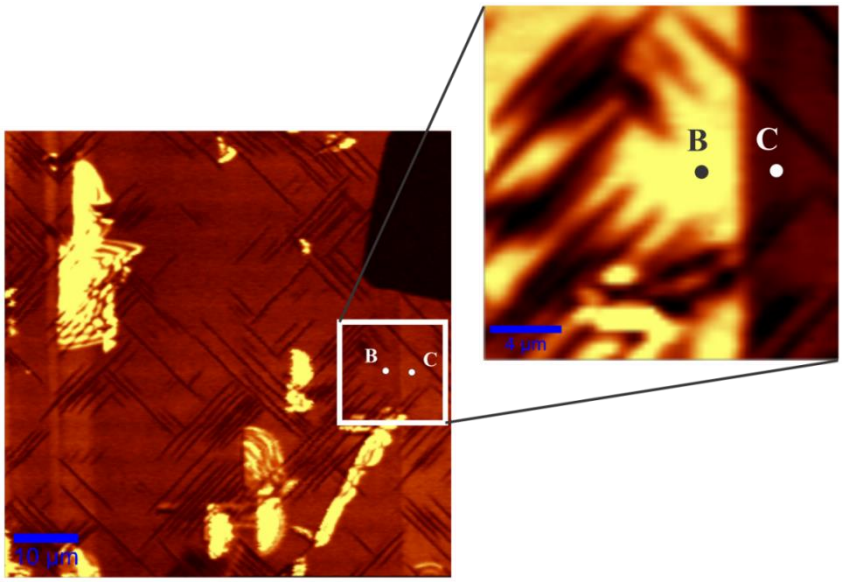

Figure 3.13: A zoomed in image of the orthorhombic regions B and C with a rescaled intensity. It is apparent that there is an intensity contrast between B and C, and that there is a vertical wall between these two regions.

Furthermore, the allowable domain walls that are along the $[010]_{pc}$ are either 90° or 180°. Since the polarizations are in the $(010)_{pc}$ face, the wall between regions B and C is a 90° domain wall, where the exact polarization directions cannot be extracted from SHG experiments. The 90° domain wall schematic is represented in **Figure 3.14**, where the direction of observation is **Z**, $[001]_{pc}$, so the 90° domain wall is a plane along $(011)_{pc}$.

An interesting discrepancy is that the theory predicts these plots to go to zero at the minima, but they do not do so in the experiment. These nonzero minima are seen in orthorhombic as well as monoclinic polar plots; they cannot be accounted for by experimental offsets, but they are due to high numerical aperture effects, discussed in Section 3.6.3.

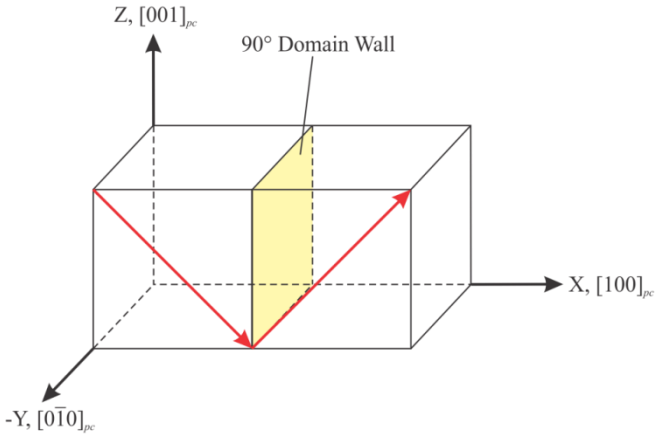

Figure 3.14: The 90° domain wall between two different domain regions with polarizations in the $(010)_{pc}$ plane. The polarizations of positions B and C are also in the $(010)_{pc}$ plane, but there are four degenerate domains in this plane, so there are other possible combinations of domains that make up a 90° domain wall. The domain wall is along the $(011)_{pc}$ plane.

3.6.2 Monoclinic Discussion

The m_2 model (Eq. 23) has a more complex form than the orthorhombic model (Eq.18) even though the qualitative shapes of the polar plots look similar. The additional offsets in the waveplate, analyzer, and sample accounted for unequal lobes seen in I_Y.

Both the m_2 and the m_1 models are able to fit the monoclinic data, but m_2 requires fewer parameters than the m_1 model. Since the m_1 model has a similar form to the m_2 model, and the m_2 model has fewer fitting parameters, the m_2 model is a better description of the monoclinic phase.

Although the polar plots of the orthorhombic and monoclinic regions have the same qualitative shape, in **Figure 3.12** the orthorhombic regions have a lower intensity than the bright monoclinic regions. Even the dark monoclinic bands have a higher intensity than that of the orthorhombic region, therefore we are certain that the polar plot regions of **Figure 3.11** are monoclinic phases. In addition, the differences in SHG intensity in the dark and bright bands are due to each region being different distortions of the orthorhombic unit cell.

The characteristic nonzero minima of the I_Y polar plots seen in the orthorhombic fitting are also seen here for the monoclinic fits of the polar plots. In both scenarios, these nonzero minima may be due to the high numerical aperture used in the data collection process in Section 3.6.3.

3.6.3 High Numerical Aperture Effects

All of the polar plots mentioned were taken using a 100x objective that has a high numerical aperture of 0.9. Since an objective focuses light onto a focal plane, the greater the angle, the larger the focusing angle. This larger focusing angle causes extraneous signal that is not accounted for in the model mentioned in Section 3.1.1, also known as the plane wave model. The plane wave model assumes that all polarization is along the **X**-**Y** plane. Yet when there is a large focusing angle, extra signal in the electric field created in the **Z**-direction ultimately contributes to the axial polarization, or P_Z. The extra signal explains the nonzero minima seen in the results.

Illustrated in **Figure 3.15**, the high numerical aperture causes a tight focusing of the incident beam. **S** is the Poynting vector, and in the direction of propagation, but it is at an angle to the **Z**-direction. Fields propagating in the **Z**-direction, or normal to the plane of the sample can be modeled using the plane wave model. On the other hand, electric fields at an angle from the normal give off signal that contributes to the polarization in the axial, **Z**-direction.

The high numerical aperture analysis done by Wang *et al*.[28], accounts for the additional axial component, P_Z. Their model considers the electric field source as a summation of radiating dipoles. In **Figure 3.16**, a dichroic mirror directs the fundamental light towards the sample. An objective lens then focuses the electric field onto a focal plane, with α_1 being the semi-angle of the lens. Since the $KNbO_3$ polarimetry experiments are in the reflection mode, the electric field is collimated after reflecting the SHG signal

back into the objective lens ($\boldsymbol{E}_1$). Finally, the field is calculated after an analyzing polarizer (at $\boldsymbol{E}_2$).

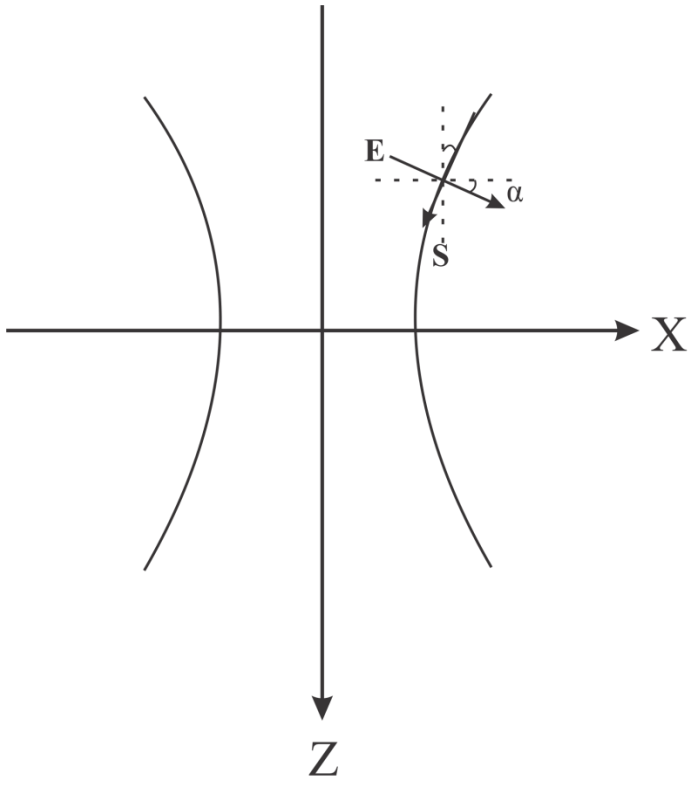

Figure 3.15: An illustration of high numerical aperture focusing that causes an extra signal in the Z-direction. S is the pointing vector, or the direction of propagation of the light, while E is the electric field that is perpendicular to S. Since E is not purely along the X-direction, there is an extra component in the Z-direction.

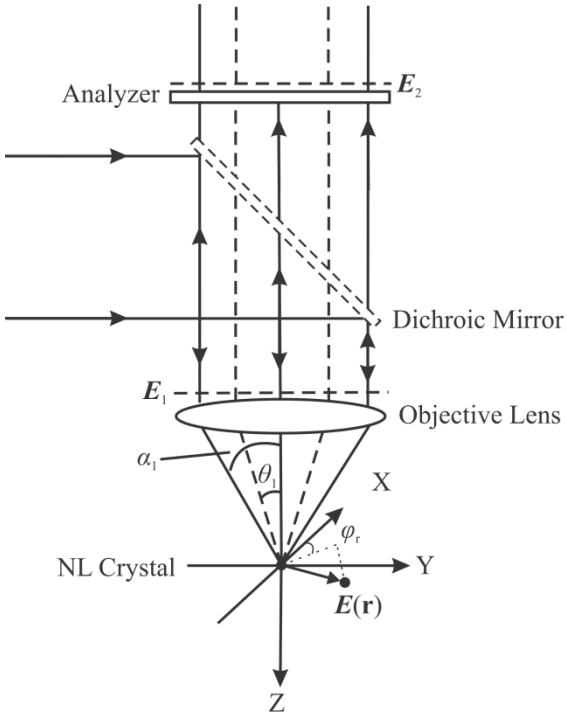

Figure 3.16: This setup is used by Wang et al. to numerically model SHG using a high numerical aperture objective. The fundamental electric field is directed onto the nonlinear crystal with the help of a dichroic mirror and a focusing lens. At the focal plane, the fundamental electric field, *E*(r), induced second harmonic generation on an excitation volume. In reflection mode, the SH signal is collimated by the objective lens, and the electric field is calculated at E_1 and again after an analyzer at E_2. The intensity after the analyzer is expressed in Eq. 34. The Witec setup uses a 100x objective, or NA = 0.9. The collimator lens is the same as the focusing lens in a reflection configuration.

Wang *et al.*'s derivation of the SH intensity is shown in Appendix A. The linearly polarized fundamental electric field at the focal region is $\boldsymbol{E}(\mathrm{r})$, which forms an azimuthal angle, φ_r, onto the X-Y plane. The induced SH polarization is a sum of the radiating dipoles in an excitation volume of the NL crystal. Given that the observation distance, R, is much greater than r, the electric fields, $\boldsymbol{E}_1$, and subsequently, the field $\boldsymbol{E}_2$ after the collimating lens, are derived. Finally, the SH intensity is

$$I = \int_0^{\alpha_1} \mathrm{d}\,\theta_1 \int_0^{2\pi} \mathrm{d}\,\varphi \left|E_2(R)\right|^2 R^2 \sin\theta_1, \tag{28}$$

where, α_1 is the semiangle of the collimating lens, which is the same as the focusing lens, R is the observation distance, and φ is the analyzer angle.

Using the derivations of Wang *et al*., the polar plots considering a high numerical aperture (0.9) was numerically generated for the orthorhombic region, B, of **Figure 3.10**. The *d*-tensor coefficients found experimentally were used in this analysis, with the exception of d_{32}, which was -27.05 pm/V.[27,24] The sample misorientations found in the Laue experiment were used in this calculation. The waveplate offset of $\Delta\phi$ = -3.00°, and the analyzer offset of $\Delta\delta$ = 3.00° were used in order to generate a high NA plot (solid line) in **Figure 3.17**. Also seen in **Figure 3.17**, the nonzero minima and the unequal lobes of the polar plots generated by the experimental and sample offsets were accounted for with a high numerical aperture model.

3.7 Conclusion

The similarity of the orthorhombic polar plots of positions B and C show that the polarizations are both on the $(010)_{pc}$ plane of the pseudo-cube. Between the two domain regions is a 90˚ wall. The exact polarizations direction cannot be determined because the intensity expressions of this plane are degenerate.

The intensity of the orthorhombic region is the lowest compared to the monoclinic dark and bright bands. There are two possible mirror planes in which the monoclinic polarizations can lie. While the monoclinic polar plots fit to both the m_2 and m_1 theoretical models, the m_2 mirror plane model best describes the monoclinic data. Furthermore, the new *d*-tensor coefficients that exist in the monoclinic phase have not been studied before,

so a direct comparison of the fit values cannot be made to any literature values. Finally, the *d*-tensor coefficients that exist in the orthorhombic phase are different in the monoclinic phase, providing further evidence that $KNbO_3$ is a two-phase system.

In the orthorhombic polar plots, the unequal lobes are due to the experimental angle offsets of the waveplate and the polarizer. Using the same offsets generated from the orthorhombic model, the high NA numerical analysis also shows unequal lobes exist in such a model. By comparing the high NA analysis to a set of orthorhombic polar plots, it is apparent that the model accounts for the observed nonzero minima. Since the high NA model takes into consideration the 100x objective, and the plane wave model does not, the high NA model is more closely describes the experiment. However, the current high NA program does not generate fit parameters, therefore more modeling work needs to be done in order to find parameters that are accurate.

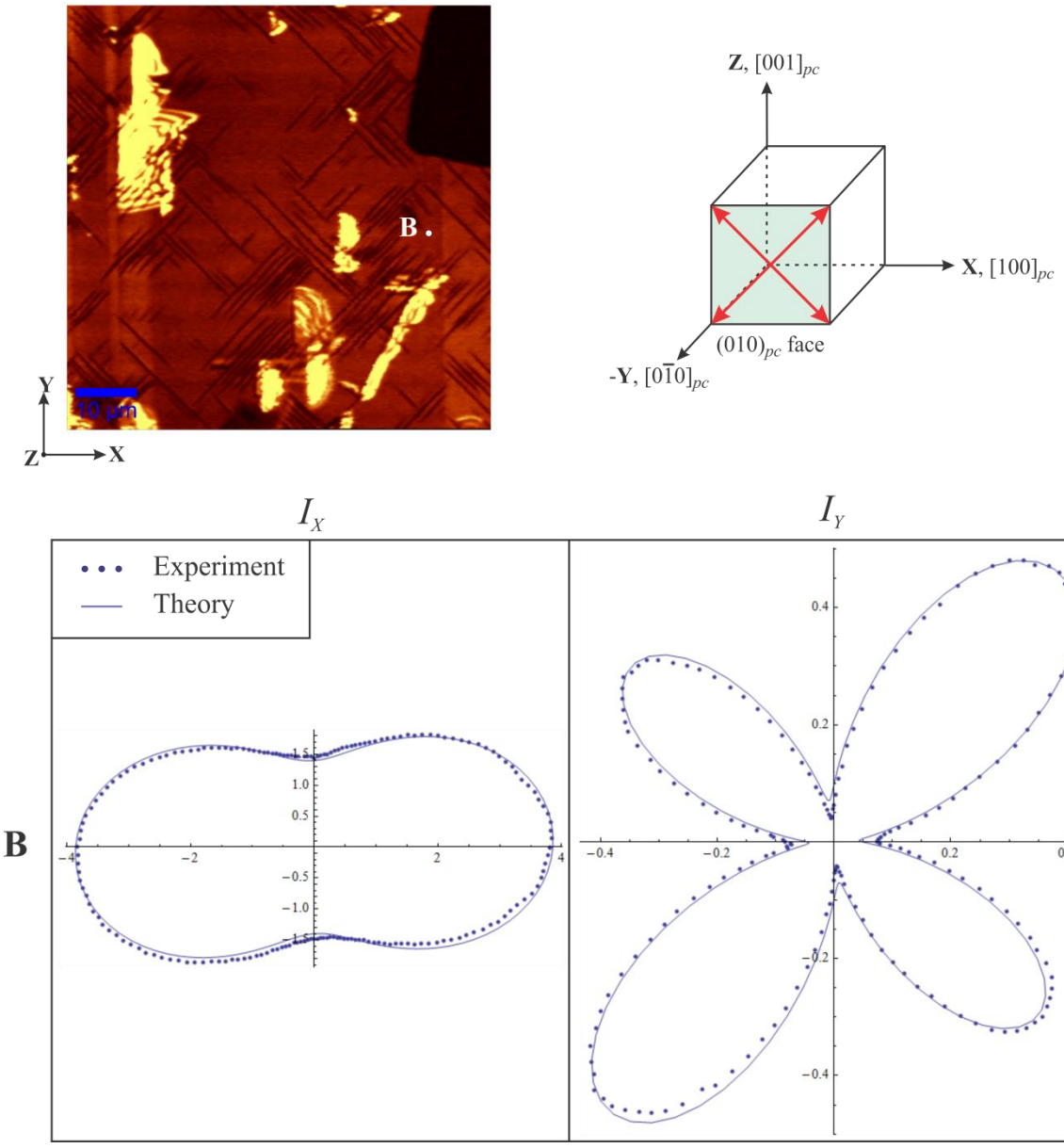

Figure 3.17: The fit of the I_X and I_Y polar plots of position B in the SHG area scan of Figure 3.9. A numerical analysis was performed using Wang et al.'s high numerical aperture model explained in Section 3.6.3. The numerical aperture of the 100x objective is 0.9. A waveplate offset $\Delta\phi$ = -3.00°, and an analyzer offset $\Delta\delta$ = 3.00° were used in this analysis. The *d*-tensor coefficient d_{32} was changed in this high NA model. As predicted, the high numerical aperture can account for the nonzero minima seen in the polar plots.

Chapter 4 Nano-scale Scanning X-Ray Diffraction Microscopy

4.1 Introduction

The nano-scale Scanning X-ray Diffraction Microscopy (nano-SXDM) experiment was performed aoutube

t beamline 26-ID-C of the Center for Nano-scale Materials (CNM) at the Advanced Photon Source at Argonne National Laboratory. The SXDM technique was performed using the Hard X-ray Nano-probe (HXN) of the CNM, which featured a diffraction-based lens (Fresnel zone plate) that focused the incident synchrotron beam to a nano-scale lateral dimension. Combined with nano-scale positioning stability, this allowed for nano-scale mapping of a specific Bragg diffraction condition, while simultaneously mapping out complimentary X-ray fluorescence data. The latter allowed for precise positioning with respect to reference markers deposited on a sample.

The SXDM technique is desirable primarily because of its nm-scale resolution.[29] Due to the high photon flux of the synchrotron source, the system also has a high signal-to-noise ratio. It can thus probe the structure of individual nano-scale domains, and do so while being nondestructive.[30,31] As such, it allows us, in principle, to probe the nano-scale structural features of the monoclinic domains in $KNbO_3$. Overall, the SXDM's experimental ability to probe domains while having high resolution and power make it a unique tool for non-invasive probing of structure on the nano-scale.

4.2 Experimental Setup

As depicted in **Figure 4.1**, a coherent and high energy X-ray beam was first generated in a double undulator. Next, the beam was redirected by a double mirror system, and then horizontally confined by an aperture. Afterward the X-ray was tuned to a wavelength of ~1.27 Å (a photon energy of 9.75 keV) by a Si crystal monochromator. A standard, transmission-type Fresnel zone plate (Xradia Inc.), composed of a 133 μm diameter gold pattern of alternating transparent and opaque concentric rings (outer ring width = 24nm, number of rings = 1385), was used to focus the monochromatic incident beam to a full width half maximum lateral beam diameter of ~30 nm. A combination of the center stop, attached to the zone plate, and a downstream aperture (before the sample), was used to block the fraction of the incident beam that passes through zone plate unaffected (zeroth order beam). The sample was placed at the focal plane, and the diffracted beam off of the sample was detected by a, 2-dimensional, area CCD detector (Princeton PIXIS-XFL 1024F), comprised of 1024 x 1024 pixels, of 13 μm^2 each. The integration time per CCD image was 1.6 seconds.

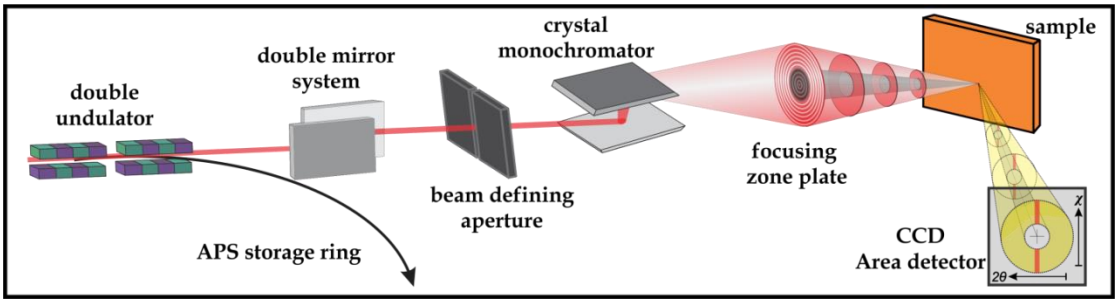

Figure 4.1: The setup of the SXDM experiment. The X-ray beam was generated by a double undulator then directed by a double mirror system, and the beam shape was defined by an aperture. The wavelength was selected by a crystal monochromator, and the focusing zone plate (also known as a Fresnel zone plate) focused the beam spot down to the nano-scale. A beam stop was attached to the zone plate, which in combination with a downstream aperture (not shown) blocks the zeroth order beam. Diffraction off of the sample was detected by a 2D CCD detector.

Figure 4.2 is a schematic top-view of the diffraction process in SXDM. The incidence angle spread of the X-ray beam (red) is ~0.32° (given by the zone plate specifications). The incidence angle, θ = 18.34°, is defined as the angle of incidence between the center of the beam and the diffraction plane, and ω is the angle between the center of the beam and the sample surface. The diffracted beam was detected by the 2D CCD area detector, centered on the diffracted beam (yellow), making an angle 2θ with the incident beam axis. The center stop used to block the zeroth order beam also blocks the center of the focused beam, leading to an annulus-like cross-section of the incident beam. As a consequence, any sample diffraction of the center portion of the incident beam will feature a similar void, as illustrated in the area detector of **Figure 4.1**. In Bragg diffraction geometry, the incident beam is not normal to the sample, so the lateral footprint is greater than 30 nm, which alters the lateral resolution of the technique. However, due to the nature of diffraction, signal from different domains require different geometric orientations, allowing for the separation of their signal, even when diffracting simultaneously.

4.3 Theory

The second harmonic generation polarimetry experiments have shown that the vertical wall in the $(011)_{pc}$ plane is a 90˚ domain wall. Although the four possible orthorhombic domain variants are in the $(010)_{pc}$ plane, there are only two different sets of diffraction planes that describe them, because X-ray diffraction is insensitive to the ferroelectric polarization. The domains are categorized as O1 or O2 domains in

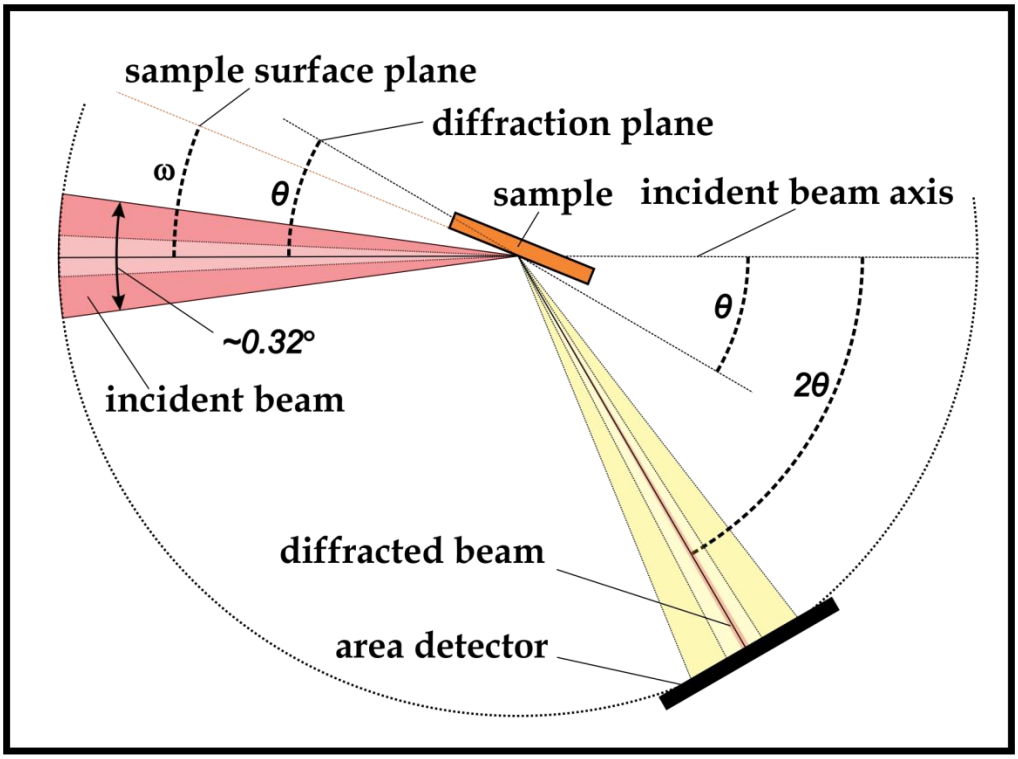

Figure 4.2: The incident X-ray beam (red) has a spread of ~0.32°. The angle of incidence, θ, is defined as the angle from the center of the incident beam to the diffraction plane. The sample surface angle, ω, is the angle between the center of the incident beam and the sample surface. The diffracted beam reaches a 2D CCD area detector. The angle 2θ is the angle formed by the diffracted beam and the incident beam (red) axis.

Figure 4.3. The lattice parameters *a*, *b*, and *c* in the *Bmm*2 description of $KNbO_3$ are listed in **Table 2.3**. Since the *a* and *c* axes have different lengths, the $\{202\}_O$ diffraction planes of the O1 domains (**Figure 4.3 a)**) and O2 domains (**Figure 4.3 b)**) oriented differently within the XZ-plane. The polarization direction is along the *c*-axis direction, so for O1, the polarization is in the $[\bar{1}01]_{pc}$ or the $[10\bar{1}]_{pc}$ direction. For the O2 domains, the polarization is in the $[101]_{pc}$ or the $[\bar{1}0\bar{1}]_{pc}$ direction. As a qualitative first approximation to the 2θ positions of the various diffracted peaks, we calculated the 2θ center of mass (COM) of the recorded CCD signal. This was done by integrating the

background-corrected CCD signal along the χ-axis (vertical axis on the detector, see **Figure 4.1**), and calculating the COM of the resulting 2θ-spectrum I_{XRD}:

$$2\theta\,COM = \frac{\sum_i 2\theta_i I_{XRD,i}}{\sum_i I_{XRD,i}}. \tag{29}$$

4.4 Results

The sample geometry was tuned to the $(202)_O$ diffraction condition. Spatial X-ray fluorescence mapping was used to find the region of interest in the sample through relative positioning with respect to a deposited grid of platinum markers. Next, a 30 x 12 μm area (labeled as "S" in **Figure 4.4 a)**) was chosen, and a $(202)_O$ Bragg diffraction map (1.6 s integration time, ~185 nm step size) probing O1 domains was recorded, as shown in **Figure 4.4 b)**. The corresponding SHG scan is shown in **Figure 4.4 a)**. Area S contains both O1 and O2 domains, but the O2 domains did not have planes that diffracted constructively in the experimental configuration due to the difference in $(202)_O$ plane orientation (refer to **Figure 4.3**, the relative angle of incidence for $(202)_O$ diffraction from the O2 domains ($\Delta\theta \approx 0.4°$) falls outside of the incidence angle spread). Representative O1 plane diffraction results are shown in **Figure 4.4 c)**, which depicts several 2D diffraction signals taken at the indicated positions (1–3). Diffraction image 1 was taken in the O1 domain, image 2 in the O2 domain, and image 3 in the O1 domain region containing monoclinic SHG signatures. The corresponding 2θ-spectra are shown below each 2D diffraction image. In order to showcase the consistency of the data in each region, additional diffraction images in each region are shown in **Appendix B**.

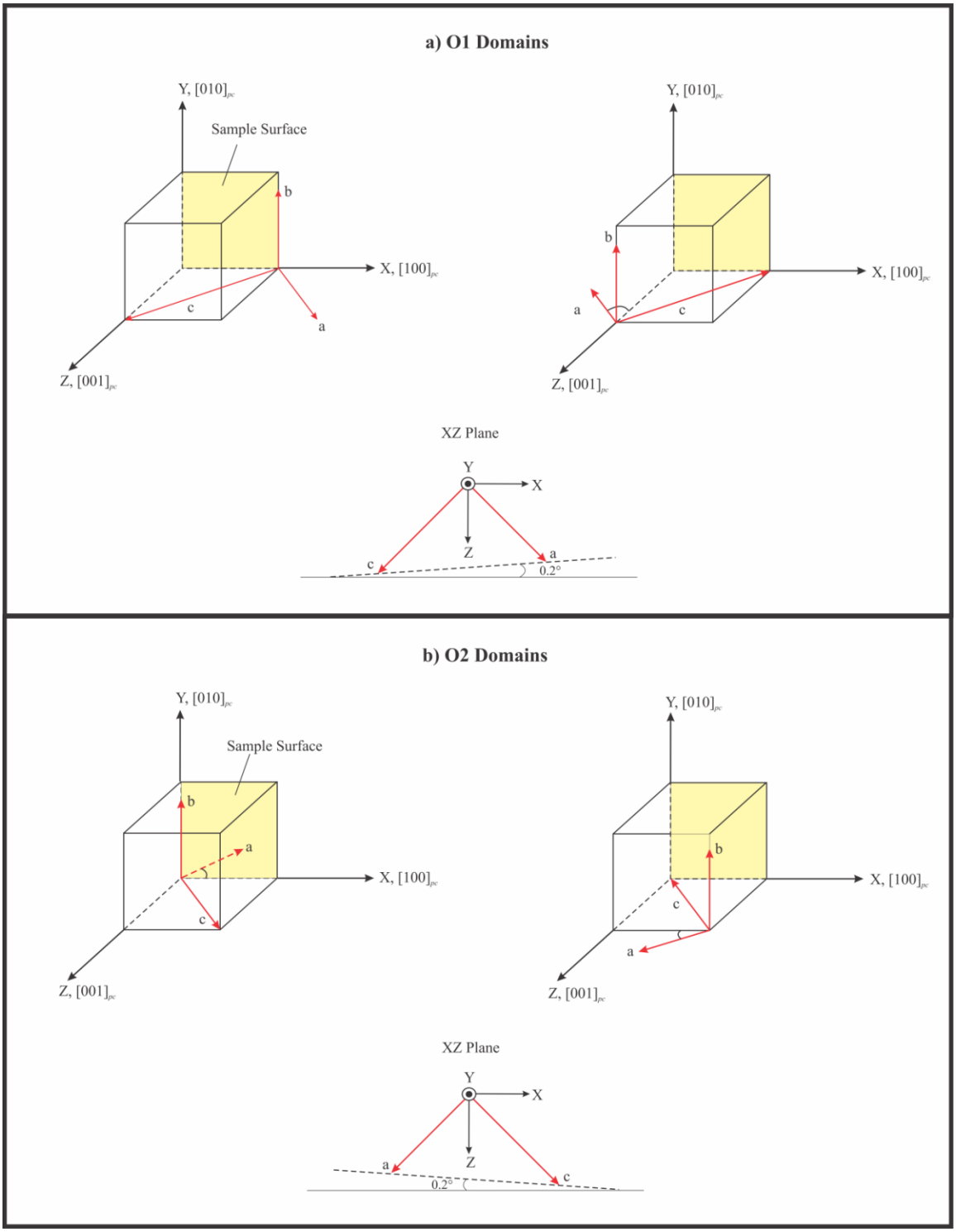

Figure 4.3: The four domain variants in the $(010)_{pc}$ plane can be grouped into two categories that have equivalently oriented diffraction planes in the XZ-plane. With *c* being the polarization direction, a) the domains having polarization in the $[\bar{1}01]_{pc}$ and the $[10\bar{1}]_{pc}$ directions are labeled O1 domains, and b) the domains having polarization in the $[101]_{pc}$ and the $[\bar{1}0\bar{1}]_{pc}$ directions are labeled O2 domains.

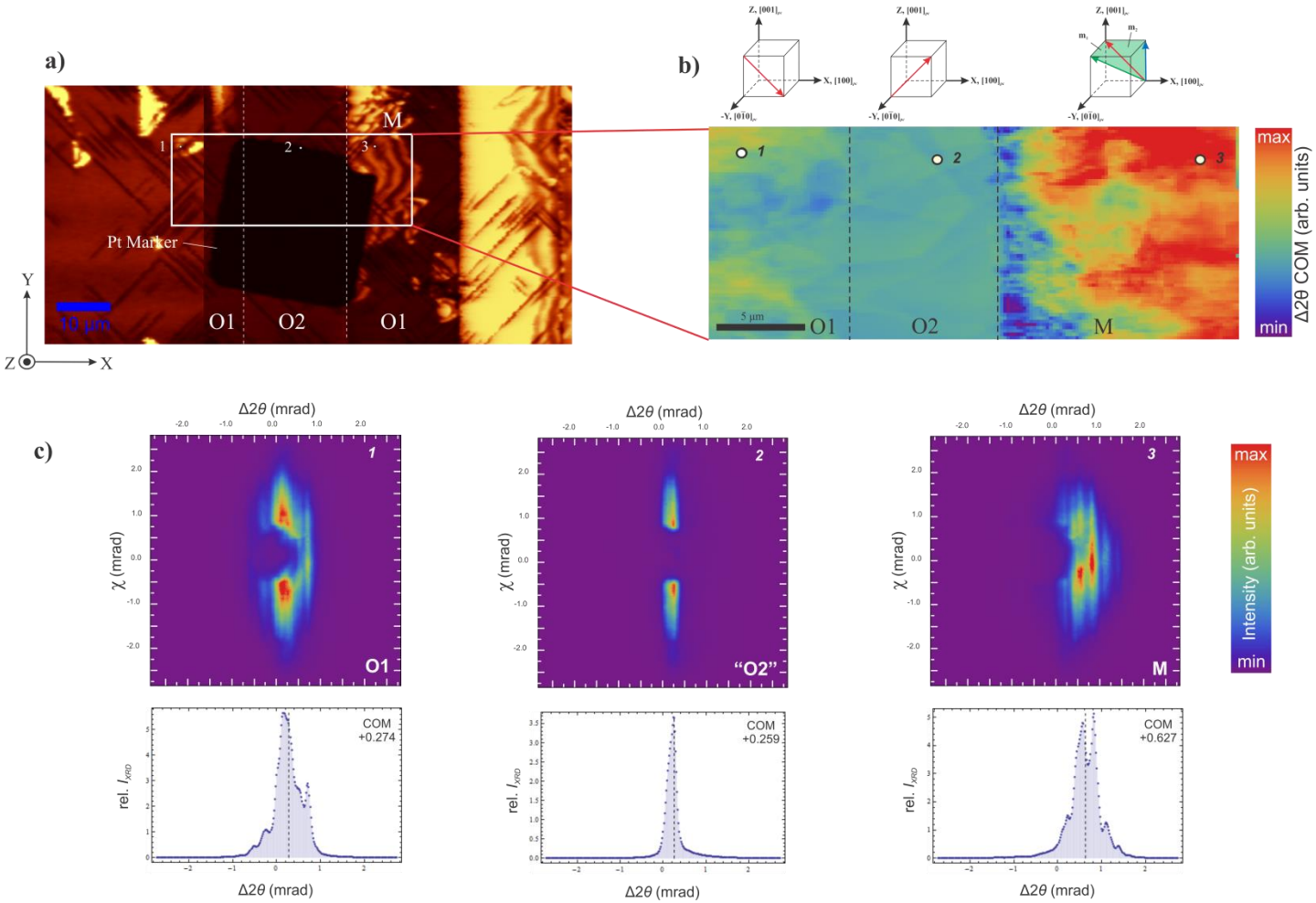

Figure 4.4: a) An SHG area scan in a $KNbO_3$ single crystal containing O1 and O2 domains, as well as a distorted O1 domain that exhibits monoclinic SHG signatures. Spatial X-ray fluorescence mapping was used to find the relative positioning of the sample with respect to a deposited grid of platinum markers. b) The corresponding spatial $\Delta 2\theta$-COM map of the $(202)_O$ Bragg diffraction recorded in area S (30 x 12 µm, 1.6 s integration time, 185 nm step size). The dashed lines indicate the 90˚ domain walls between O1 and O2 domains, and numbered positions refer to 2D diffraction images shown in c). c) Representative 2D diffraction images from the three domains. Image 1 was taken in the pure O1 region, image 2 was taken in the O2 region, and image 3 was taken in the monoclinic (distorted O1) region. The corresponding 2θ spectrum is shown below each of the diffraction images, with the centers of mass, as calculated using Eq. 35, indicated by the dashed lines. Note that the 2θ value is relative to the center of the CCD image

4.5 Discussion

In comparing the SHG area scan (**Figure 4.4 a)**) and the spatial $\Delta 2\theta$-COM map of the $(202)_O$ Bragg diffraction (**Figure 4.3 b)**), one can see that there is a correlation between the monoclinic SHG signatures and the relative 2θ value of the $(202)_O$ diffraction. The domain region that exhibits monoclinic fringes in the SHG scan consistently shows a higher relative 2θ value, as compared to the pure O1 region. This is clearly reflected by the apparent domain wall in the Bragg diffraction map. The diffraction signal observed in the O2 region, presumably originates from deeper-lying O1 domains, which are simultaneously illuminated due to the penetration depth of ~9.07 μm, and the angle of incidence. The center of mass of this contribution is similar to that observed in the pure O1 region. Nevertheless, the spatial $\Delta 2\theta$ -COM map features three distinct regions, which is also supported by the 2D diffraction images and the 2θ spectra.

The 2D diffraction image 1 of **Figure 4.3 c)**, taken in the pure O1 domain region, exhibits multiple peaks, indicating that there are structural variations within the probing volume. These variations may be due to either slightly different orientations, or slight relative distortions of O1 domains diffracting from different probing depths. However, the corresponding relative 2θ COM is consistent within the pure O1 region at ~0.30 mrad (0.017º), indicating that the main contribution to the O1 diffraction is uniform. As expected, in the O2 region (image 2), the O1 diffraction is much weaker, as the diffraction signal observed here originates from the reduced volume that probes deeper lying O1 domains only. This is also consistent with the observed relative 2θ COM of ~0.30 mrad (0.017º) in the O2 region, as shown in Appendix B, by the additional diffraction images in the three regions. The 2D diffraction image in the monoclinic

region (image 3) exhibits multiple peaks similar to those observed in the pure O1 region, indicating similar variations at different depths within the probing volume. Also here, the relative 2θ COM is consistent within the region, but it is shifted to ~0.65 mrad (0.037º). As shown by the contrast in **Figure 4.4 b)**, this relative 2θ shift strongly correlates with the monoclinic SHG signatures in the complementary SHG scan (**Figure 4.4 a)**).

4.6 Conclusion

The pure O1 domain using the $(202)_O$ diffraction condition was probed using nano-SXDM. The spatial $\Delta 2\theta$ COM Bragg diffraction map exhibits three distinct domains (pure O1, O2, and O1 with monoclinic features) whose differences were further supported by the extracted $\Delta 2\theta$ spectra. The multiple peaks in the diffraction images are due to either the distortions or the structural variations in the O1 domains. The COMs of both the O1 and the O2 domain regions are similar because the probing volume in the O2 region contains underlying O1 domains. The O1 region with monoclinic features has COMs that are shifted from those of the pure O1 region. The qualitative conclusion based upon this trend is that the structure in the area with SHG fringes is distorted from that of the conventional orthorhombic O1 domains. Quantifying the degree and the nature of this distortion will require additional X-ray experiments and analysis.

Chapter 5 Conclusion and Future Work

5.1 Conclusion

By using the optical second harmonic generation (SHG) experimental technique, the sets of polarization directions of domains can be determined. Extracted from the modeling of the orthorhombic domains, the inclusion of experimental offsets in the waveplate and the analyzer, as well as the sample misorientation due to polishing is required in order to correctly model the polar plot data. The offsets account for the unequal lobes that arise in the polar plots, and were also used in the monoclinic data analysis.

For the first time, monoclinic domains in $KNbO_3$ were studied using optical SHG. The monoclinic domains have enhanced nonlinear responses that were observed through the increase in intensity compared to those of the orthorhombic domains. In addition to the higher SHG intensity being a signature to the monoclinic domains, nano-scale scanning X-ray diffraction microscopy data reveals a difference in center-of-mass values between the monoclinic and the orthorhombic domains. Furthermore, the corresponding images indicate that the monoclinic domains contain distortions to the orthorhombic structure.

The polar plot data of the orthorhombic and monoclinic domains have nonzero minima that are not predicted by the plane wave model. By implementing the high numerical aperture (NA) technique, the high numerical aperture focusing lens is considered and corrects for the nonzero minima. Although the parameters used in the high NA model are not the same as those generated from the plane wave fit, the high NA model better describes the actual experimental setup.

5.2 Future Work

The monoclinic domains may be due to shearing of the lattice structure of $KNbO_3$. In order to verify the shearing model, a more quantitative approach to studying the monoclinic nano-SXDM data can be used to determine the types of distortions that arise in the orthorhombic structure in order to obtain the monoclinic phases. By analyzing the individual peaks in the diffraction images, information on shearing in the monoclinic domains can be extracted.

Currently the high NA model is a numerical analysis program, but by creating a fitting model out of this analysis the best fit parameters can be extracted to more accurately describe the experimental setup. A study of the polar plots using a variety of numerical apertures can aid the process of modeling the system with a focusing objective by testing the program's robustness. With a working fitting program, the high NA model can extend to fitting monoclinic polar plots, as well as polar plots of domains in the other phases of $KNbO_3$.

As monoclinic phases have been detected in the orthorhombic phase, it may also exist in the rhombohedral and tetragonal phases. Temperature varying SHG experiments would be required in order to detect the monoclinic phases at different crystal structures. A temperature controller will need to be installed onto the sample stage of the Witec microscope in order to maintain a constant phase.

References

1. Maeder, M. D., Damjanovic, D. & Setter, N. Lead Free Piezoelectric Materials. *Journal of Electroceramics* **13**, 385–392 (2004).

2. Lummen, T. T. A., Barnes, E., Gu, Y., Chen, L.-Q. & Gopalan, V. Bridging states with enhances properties through interface engineering. (2012).

3. Lummen, T. T. A. *et al.* Direct Imaging of an Emergent Ferroelectric Phase with Enhanced Properties.

4. Liang, L., Li, Y. L., Hu, S. Y., Chen, L.-Q. & Lu, G.-H. Piezoelectric anisotropy of a KNbO3 single crystal. *Journal of Applied Physics* **108**, 094111 (2010).

5. Park, S.-E., Wada, S., Cross, L. E. & Shrout, T. R. Crystallographically engineered BaTiO[sub 3] single crystals for high-performance piezoelectrics. *Journal of Applied Physics* **86**, 2746 (1999).

6. Prokhorov, A. M. & Kuz'minov, Y. S. Single Crystals of Potassium Niobate. *Ferroelectric Crystals for Laser Radiation Control* 5–29 (1990).

7. Shirane, G., Danner, H., Pavlovic, A. & Pepinsky, R. Phase Transitions in Ferroelectric KNbO3. *Physical Review* **93**, 672–673 (1954).

8. Gopalan, V. & Raj, R. Domain Structure-Second Harmonic Generation Correlation in Potassium Niobate thin films on Strontium Titanate substrates.pdf. *Journal of the American Ceramic Society* **79**, 3289–3296 (1996).

9. Deshmukh, K. G. & Ingle, S. G. Interferometric studies of domain structures in potassium niobate single crystals. *Journal of Physics D: Applied Physics* **4**, 124–132 (1971).

10. Denev, S. A., Lummen, T. T. A., Barnes, E., Kumar, A. & Gopalan, V. Probing Ferroelectrics Using Optical Second Harmonic Generation. *Journal of the American Ceramic Society* **94**, 2699–2727 (2011).

11. Katz, L. & Megaw, H. The Structure of Potassium Niobate at Room Temperature: The Solution of a Pseudosymmetric Structure by Fourier Methods. *Acta Crystallographica* **22**, 639–648 (1967).

12. Kittel, C. Chapter 2: Wave Diffraction and the Reciprocal Lattice. *Introduction to Solid State Physics* 24–26 (2005).

13. Ashcroft, N. W. & Mermin, N. D. Determincation of Crystal Structures by X-ray Diffraction. *Solid State Physics* 96–97 (1976).

14. Li, S., Ahuja, R. & Johansson, B. Pressure-induced phase transitions of KNbO3. *Journal of Physics: Condensed Matter* **14**, 10873–10877 (2002).

15. Yamanaka, T., Okada, T. & Nakamoto, Y. Electron density distribution and static dipole moment of KNbO3 at high pressure. *Physical Review B* **80**, 094180–1 (2009).

16. Boyd, R. W. The Nonlinear Optical Susceptibility. *Nonlinear Optics* 4–12 (2003).

17. Boyd, R. W. The Nonlinear Optical Susceptibility. *Nonlinear Optics* 1–3 (2003).

18. Newnham, R. E. *Properties of Materials: Anisotropy, Symmetry, Structure*. 34–35, 92, 313–317 (Oxford University Press: New York, 2009).

19. Spectra-Physics *Tsunami: Mode-Locked Ti:sapphire Laser*. (1999).

20. Spectra-Physics *Millennia Xs: Diode-pumped, cs Visible Laser*. (2000).

21. Herman, W. N. & Hayden, L. M. Maker fringes revisited: second-harmonic generation from birefringent or absorbing materials. *Journal of the Optical Society of America B* **12**, 416 (1995).

22. Haislmaier, R. In preparation.

23. Zysset, B., Biaggio, I. & Gunter, P. Refractive indices of orthorhombic KNbO3. I. Dispersion and temperature dependence. *Journal of the Optical Society of America B* **9**, 380386 (1992).

24. Biaggio, I., Kerkoc, P., Wu, L.-S. & Gunter, P. Refractive indices of orthorhombic KNbO3. II. Phase-matching configurations for nonlinear-optical interactions. *Journal of the Optical Society of America B* **9**, 507–517 (1992).

25. Shoji, I. Absolute scale of second-order nonlinear optical coefficients. *Journal of the Optical Society of America B* **14**, 2268–2294 (1997).

26. Gopalan, V. Light in Anisotropic Media.

27. Baumert, J.-C., Hoffnagle, J. & Gunter, P. Nonlinear optical effects in KNbO3 crystals at Al(x)Ga(1-x)As, dye, ruby and Nd:YAG laser wavelength. *1984 European Conference on Optics, Optical Systems, and Applications* **492**, 374–385 (1984).

28. Wang, X.-H. *et al.* Vector model for polarized second-harmonic generation microscopy under high numerical aperture. *Journal of Optics* **12**, 045201 (2010).

29. Xiao, Y., Cai, Z., Wang, Z. L., Lai, B. & Chu, Y. S. An X-ray nanodiffraction technique for structural characterization of individual nanomaterials. *Journal of synchrotron radiation* **12**, 124–8 (2005).

30. Hruszkewycz, S. O. *et al.* X-ray nanodiffraction of tilted domains in a poled epitaxial BiFeO3 thin film. *Applied Physics Letters* **99**, 232903 (2011).

31. Keckes, J. *et al.* X-ray nanodiffraction reveals strain and microstructure evolution in nanocrystalline thin films. *Scripta Materialia* **67**, 748–751 (2012).

Appendix A

According to Wang et al., the linearly polarized fundamental electric field at the focal region is,

$$\begin{aligned} E_X(r) &= -iA\left[I_0 + I_2\cos(2\varphi_r)\right] \\ E_Y(r) &= -iAI_2\sin(2\varphi_r) \\ E_Z(r) &= -2AI_1\cos(\varphi_r), \end{aligned} \tag{30}$$

where φ_r is the azimuthal angle of the electric field at a point *r*. *A* is proportional to the electric field amplitude. The terms I_n are the Richards and Wolf integrals, defined as,

$$I_0 = \int_0^{\alpha_1} \cos^{1/2}\theta_1 \sin\theta_1 (1+\cos\theta_1) J_0(kr\sin\theta_1)\exp(ikz\cos\theta_1)\,\mathrm{d}\theta_1$$

$$I_1 = \int_0^{\alpha_1} \cos^{1/2}\theta_1 \sin^2\theta_1 J_1(kr\sin\theta_1)\exp(ikz\cos\theta_1)\,\mathrm{d}\theta_1$$

$$I_2 = \int_0^{\alpha_1} \cos^{1/2}\theta_1 \sin\theta_1 (1-\cos\theta_1) J_2(kr\sin\theta_1)\exp(ikz\cos\theta_1)\,\mathrm{d}\theta_1, \tag{31}$$

where J_n are Bessel functions of the order *n*. The term α_1 is the angle defined by the numerical aperture equation, $NA = n\sin(\alpha_1)$, where *n* is the index of the medium in which the lens is subsiding (in this case, $n_{air} = 1.0$).

The induced SH polarization is a sum of the radiating dipoles in an excitation volume of the NL crystal. Given that the observation distance, *R*, is much greater than *r*, the electric field at the plane $\boldsymbol{E}_1$ after the collimating lens of **Figure 3.16** is

$$\begin{aligned} E_{1X} &= \cos^{-1/2}\theta_1\left(-a_1B_X - a_2B_Y + a_3B_Z\right) \\ E_{1X} &= \cos^{-1/2}\theta_1\left(-a_2B_X - a_4B_Y + a_5B_Z\right) \\ E_{1Z} &= 0, \end{aligned} \tag{32}$$

where a_n is the weight factor of the NL polarization appearing in the terms, B_X, B_Y, and B_Z.

$$
\begin{aligned}
a_1 &= \sin^2\varphi + \cos^2\varphi\cos\theta_1 \\
a_2 &= \sin\varphi\cos\varphi(\cos\theta_1 - 1) \\
a_3 &= \sin\varphi\sin\theta_1 \\
a_4 &= \sin^2\varphi\cos\theta_1 + \cos^2\varphi \\
a_5 &= \sin\varphi\sin\theta_1 \\
B_X &= \frac{\exp(2ikR)}{4\pi R}\int_{\upsilon}\exp(-2iks\cdot r)\,p_x\,\mathrm{d}^3r \\
B_Y &= \frac{\exp(2ikR)}{4\pi R}\int_{\upsilon}\exp(-2iks\cdot r)\,p_Y\,\mathrm{d}^3r \\
B_Z &= \frac{\exp(2ikR)}{4\pi R}\int_{\upsilon}\exp(-2iks\cdot r)\,p_Z\,\mathrm{d}^3r
\end{aligned}
\tag{33}
$$

The SH polarizations are p_X , p_Y , and p_Z are derived from Eq. 5. The angle φ is the azimuthal angles of the observation point $\boldsymbol{R}$, respectively.

The electric field at the plane $\boldsymbol{E}_2$, behind the analyzer at an angle φ is

$$
\begin{aligned}
E_{2X} &= \cos^2\psi E_{1X} + \sin\psi\cos\psi E_{1Y} \\
E_{2Y} &= \cos\psi\cos\psi E_{1X} + \sin^2\psi E_{1Y} \\
E_{2Z} &= 0.
\end{aligned}
\tag{34}
$$

Finally, the SH intensity is

$$
I = \int_0^{\alpha_1}\mathrm{d}\theta_1\int_0^{2\pi}\mathrm{d}\varphi\left|E_2(R)\right|^2 R^2\sin\theta_1, \tag{35}
$$

where, α_1 is the semiangle of the collimating lens, which is the same as the focusing lens.

Appendix B

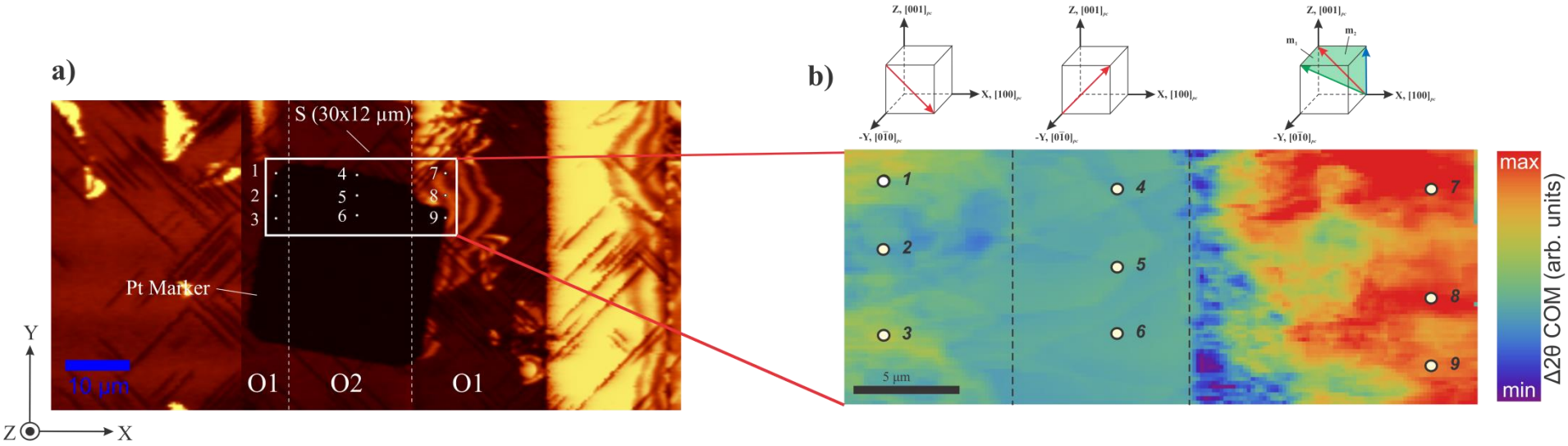

a) An SHG area scan in a $KNbO_3$ single crystal containing O1 and O2 domains, as well as a distorted O1 domain that exhibits monoclinic SHG signatures. Spatial X-ray fluorescence mapping was used to find the relative positioning of the sample with respect to a deposited grid of platinum markers. b) The corresponding spatial $\Delta 2\theta$-COM map of the $(202)_O$ Bragg diffraction recorded in area S (30 x 12 µm, 1.6 s integration time, 185 nm step size). The dashed lines indicate the 90˚ domain walls between O1 and O2 domains, and numbered positions refer to 2D diffraction images shown in c). c) Representative 2D diffraction images from the three domains. Images 1–3 were taken in the pure O1 region, images 4–6 were taken in the O2 region, and images 7–9 were taken in the monoclinic (distorted O1) region. The corresponding 2θ spectrum is shown below each of the diffraction images, with the centers of mass, as calculated using Eq. 35, indicated by the dashed lines. Note that the 2θ value is relative to the center of the CCD image.

c)

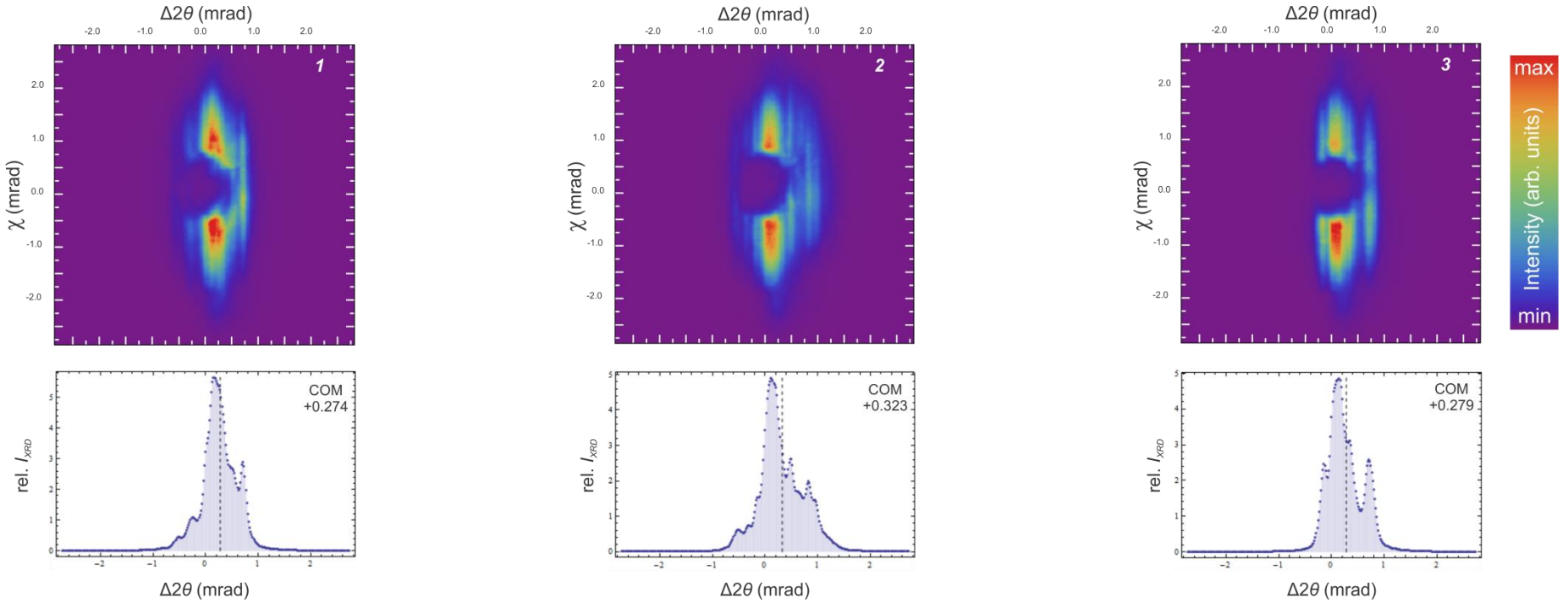
Δ2θ (mrad)
χ (mrad)
1
2
3
max
Intensity (arb. units)
min
rel. I_XRD
COM
+0.274
+0.323
+0.279

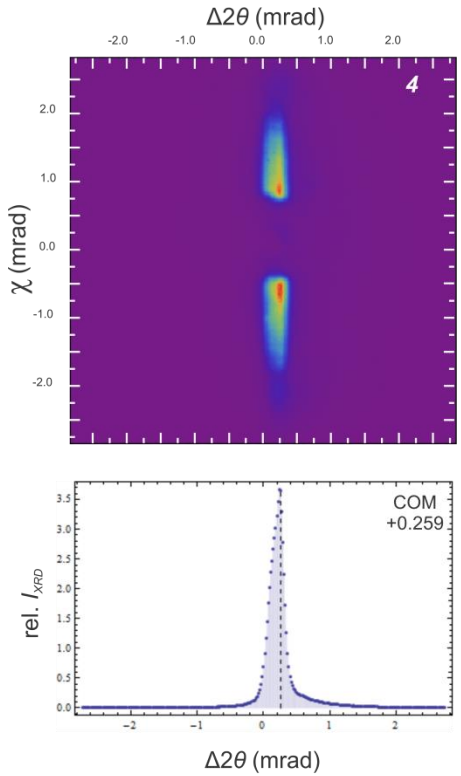
Δ2θ (mrad)
-2.0 -1.0 0.0 1.0 2.0
4
χ (mrad)
2.0 1.0 0.0 -1.0 -2.0
COM
+0.259
rel. I_{XRD}
Δ2θ (mrad)

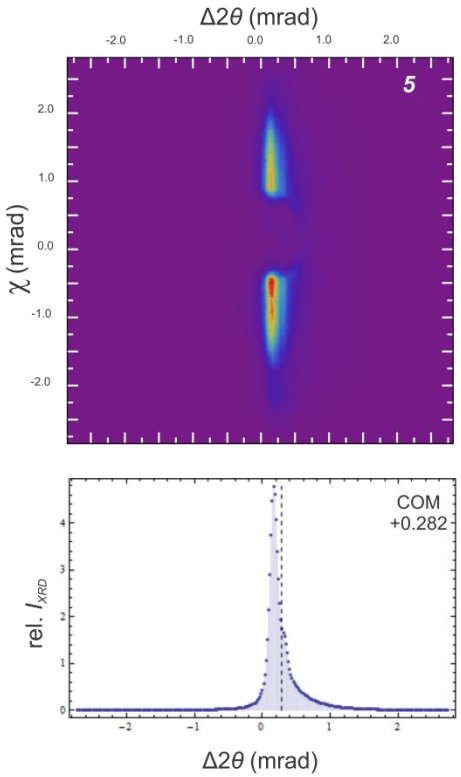
Δ2θ (mrad)
-2.0 -1.0 0.0 1.0 2.0
5
χ (mrad)
2.0 1.0 0.0 -1.0 -2.0
COM
+0.282
rel. I_{XRD}
Δ2θ (mrad)

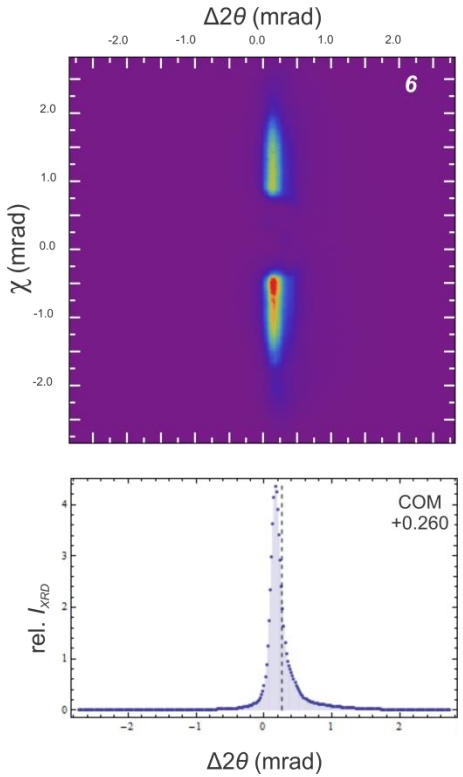
Δ2θ (mrad)
-2.0 -1.0 0.0 1.0 2.0
6
χ (mrad)
2.0 1.0 0.0 -1.0 -2.0
COM
+0.260
rel. I_{XRD}
Δ2θ (mrad)

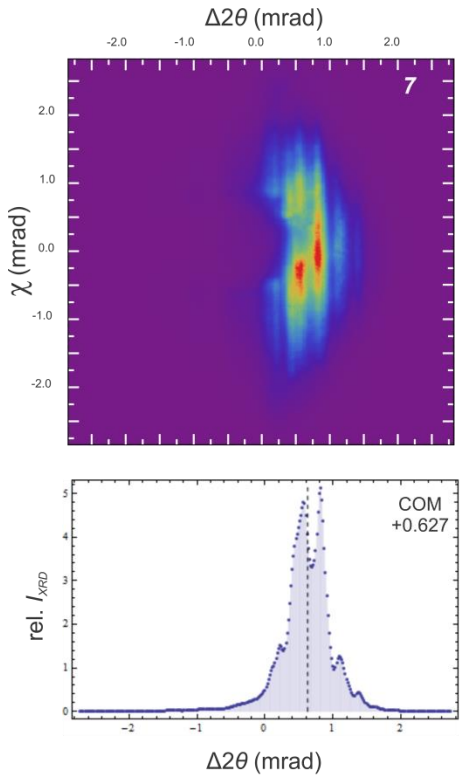
Δ2θ (mrad)
-2.0 -1.0 0.0 1.0 2.0
7
χ (mrad)
2.0 1.0 0.0 -1.0 -2.0
COM
+0.627
rel. I_{XRD}
Δ2θ (mrad)

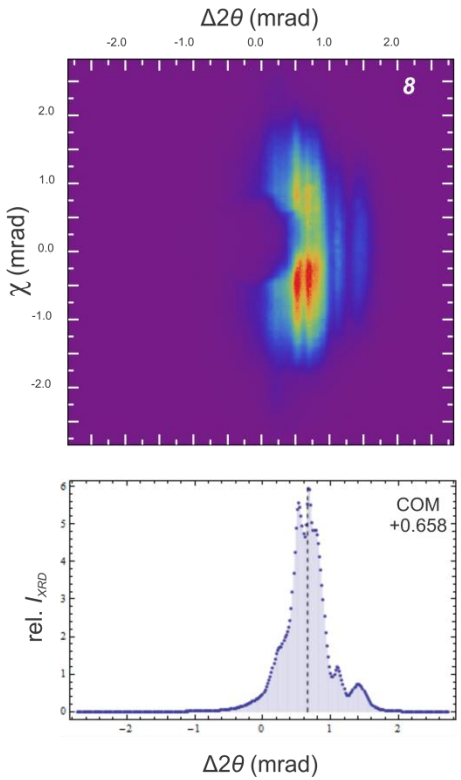
Δ2θ (mrad)
-2.0 -1.0 0.0 1.0 2.0
8
χ (mrad)
2.0 1.0 0.0 -1.0 -2.0
COM
+0.658
rel. I_{XRD}
Δ2θ (mrad)

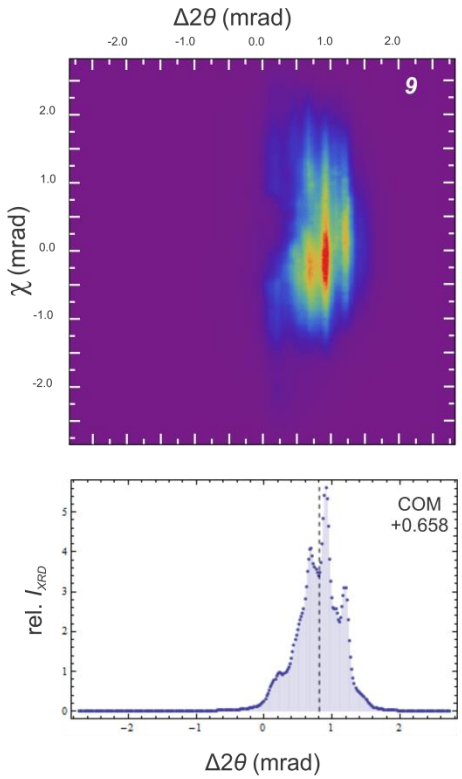
Δ2θ (mrad)
-2.0 -1.0 0.0 1.0 2.0
9
χ (mrad)
2.0 1.0 0.0 -1.0 -2.0
COM
+0.658
rel. I_{XRD}
Δ2θ (mrad)